Supporting Information for

Multi-spatial scale assessment and multi-dataset fusion of global terrestrial evapotranspiration datasets

Contents of this file

Text S1–S6
Figures S1–S25
Tables S1–S5

Text S1. Flux sites and data preprocessing

The ET from FLUXNET has been quality controlled and pre-processed to improve cross-site consistency and comparability using the harmonised methodology described in Pastorello et al. (2020). Meteorological data were filled by two independent methods: marginal distribution sampling (variables with _F_MDS suffix) and ERA-Interim (variables with _F_ERA suffix). The final missing-fill product (variables with _F suffix) consists of direct measurements and missing-fill records. In this study, latent heat fluxes were filled using half-hourly (hourly) precipitation (P_F in mm) and MDS methods (LE_F_MDS in $W \cdot m^{-2}$). Record lengths for each site ranged from 1 to 24 years. For latent heat fluxes, the data processing steps (screening criteria) were as follows: (1) First, only data with a continuous coverage of at least 3 years were collected. (2) Data with negative latent heat fluxes were excluded. (3) Because flux data from nighttime eddy covariance measurements are missing and have large errors (Mahrt, 1999; Yuan et al., 2021), the study extracted only daytime latent heat flux data. Daytime is defined as 7:00 to 19:00 local time (McGloin et al., 2019; Yuan et al., 2021). The study did not use incident shortwave radiation to define daytime, as nighttime occasionally has larger values. (4) To avoid high likelihood of dew evaporation (Knauer et al., 2018), the study excluded data with relative humidity above 95%, as it can strongly affect evapotranspiration measurements. (5) To avoid intercepted evaporation and sensor saturation at high relative humidity (Medlyn et al., 2017), data during and up to 6 hours after rainfall were excluded. (6) To reduce the impact of outliers on half-hourly-scale data, data below the 5% percentile and above the 95% percentile in latent heat flux were excluded. Half-hourly evapotranspiration (in mm) was obtained from the latent heat flux calculations. For precipitation, only (2) and (6) were considered in the data processing steps. Half-hourly data (precipitation and evapotranspiration) were finally computed on a monthly scale. In the end, 174 stations were retained.

Text S2. Verification of energy balance closure

There are many computational methods for evaluating and analysing energy balance closure, and in order to be able to comprehensively evaluate the state of energy balance closure at each flux site, this study used the least-squares linear regression (ordinary least squares [OLS]) and the energy balance ratio (EBR) methods. The study adjusted some of the flux data to ensure the quality of the data used in this study. Site energy closure is a key indicator of flux data quality (Zhu et al., 2016).

$$Res = R_n - H - \lambda E - G \tag{S1}$$

where R_n is the net radiation (W·m^{-2}), H is the sensible heat flux (W·m^{-2}), λE is the latent heat flux (W·m^{-2}), and G is the soil heat flux (W·m^{-2}). The difference between net radiation and soil heat flux is the available energy. In most cases, the available energy is greater than the sum of sensible and latent heat. In general, the surface energy balance closure (the sum of sensible and latent heat fluxes divided by the available energy) is usually in the range of 70% to 90% (Foken et al., 2006).

Text S3. Water balance method

At the basin scale, changes in precipitation, runoff, ET, and total water storage constitute the watershed water balance, and the variables in the water balance can be obtained relatively accurately except for ET; therefore, watershed ET is usually calculated using the water balance method, and the method is often used as a standard method for watershed ET estimation (Xu et al., 2019). Based on the water balance principle, the actual evapotranspiration is calculated using the following equation

$$ET = P - R - TWSC \tag{S2}$$

where P represents total precipitation in the basin, R represents total runoff in the basin, and $TWSC$ represents the change in total water storage. Basin ET values obtained based on water balance are often used as reference values to verify the accuracy of ET datasets at the basin scale (Senay et al., 2011; Zhang et al., 2010). Equation 2 can be used to assess various global ET datasets in a basin but is not applicable to the basins where R is not available. TWSC should be considered when data span less than 10 years, especially for monthly-scale ET assessments. The formula for the region is as follows:

$$TWSC(i) = \frac{TWSA(i+1) - TWSA(i-1)}{2\Delta i} \tag{S3}$$

Here, $TWSA$ is the total water storage anomaly, which can be obtained from GRACE data(Tapley et al., 2019). When the data spans more than 10 years, it can be ignored. Thus, the above equation can be written as $ET = P - R$.

Text S4. Three-cornered hat (TCH) method

The study uses the three-cornered hat (TCH) method to calculate the errors and uncertainties of thirty evapotranspiration datasets without any prior knowledge.

67

68 The details of the TCH method are described below. Assuming that there are n

69 different evapotranspiration datasets $\{ET_i\}_{i=1,2,\dots,N}$, i, then the ith ET dataset ET_i

70 can generally be expressed as

$$ET_i = ET_{true} + \varepsilon_i, i = 1,2,\dots,n \tag{S4}$$

72 Among them, ET_{true} is the true surface ET, and ε_i is the observation error of ET_i.

73 Since the real ET value cannot be obtained, any ET dataset is selected as the reference

74 value, and the difference sequence between the remaining ET datasets and the reference

75 value is obtained as

$$y_i = ET_i - ET_{ref} = \varepsilon_i - \varepsilon_{ref}, i = 1,2,\dots,n-1 \tag{S5}$$

77 ET_{ref} is an arbitrarily selected reference ET dataset. The error analysis results of the

78 TCH method do not depend on the selection of the reference dataset (Ferreira et al.,

79 2016). The covariance matrix of Y can be represented by $S = cov(Y)$. Introducing the

80 unknown noise covariance matrix R (R is a symmetric matrix), then its relationship

81 with S is

$$S = J \cdot R \cdot J^T \tag{S6}$$

83 where J is represented as

$$J_{n-1,n} = \begin{bmatrix} 1 & 1 & \cdots & 0 & -1 \\ 0 & 0 & \cdots & 0 & -1 \\ \vdots & \vdots & \ddots & \vdots & \vdots \\ 0 & 0 & 0 & \cdots & -1 \end{bmatrix} \tag{S7}$$

85 Matrix R is defined as

$$R = \begin{bmatrix} \sigma_{11} & \sigma_{12} & \cdots & \sigma_{1n} \\ \sigma_{12} & \sigma_{22} & \cdots & \sigma_{21} \\ \vdots & \vdots & \ddots & \vdots \\ \sigma_{1n} & \sigma_{21} & \cdots & \sigma_{nn} \end{bmatrix} \tag{S8}$$

87 Among these, $\sigma_{ii} = cov(\varepsilon_i, \varepsilon_j)$, $(i, j = 1, 2, \cdots, n)$, is the covariance of time series ε_i

88 and ε_j. However, Eq. (8) cannot be solved as the number of unknown elements is larger

89 than the number of equations. Therefore, the remaining parameters require a reasonable

90 approach to obtain a unique value. Galindo and Palacio (1999) proposed a method

91 based on Kuhn-Tucker theory, and the objective function is given below:

$$92 \qquad\qquad F_{(\sigma_{1n},\ldots,\sigma_{nn})} = \frac{1}{K^2}\sum_{i<j}^{n}(\sigma_{ij})^2 \qquad\qquad\qquad (S9)$$

93   Here, $K = \sqrt[N-1]{\det(S)}$. The constraint H is

$$94 \qquad\qquad H_{(\sigma_{1n},\ldots,\sigma_{nn})} = -\frac{|Q|}{|S|\cdot K} < 0 \qquad\qquad\qquad (S10)$$

95   Q is a diagonal matrix, and the elements on its diagonal are $\sigma_{11}, \sigma_{22}, \ldots, \sigma_{nn}$. The

96   square root of the Q diagonal values are considered to be the uncertainty of evaluated

97   ET. The ratio of the uncertainty to the time series mean value is the relative uncertainty.

98

99   **Text S5. Bayesian model average (BMA) fusion scheme**

100   Bayesian model averaging (BMA) has recently been proposed as a statistical method

101   to calibrate forecast ensembles from numerical weather models. Successful

102   implementation of BMA, however, requires accurate estimates of the weights and

103   variances of the individual competing models in the ensemble. In this study, we use the

104   DiffeRential Evolution Adaptive Metropolis (DREAM) Markov Chain Monte Carlo

105   (MCMC) algorithm for estimating the BMA weights and variances (Vrugt et al., 2008).

106   The formulas are described in detail in Vrugt et al. (2008).

107

108   **Text S6. Weighting scheme for ET dataset fusion**

109   Analysis was performed based on the grid scale of each ET dataset. Among these

110   datasets, 1982–2011 are the common coverage years for all ET datasets, and their

111   weights are calculated as detailed in section 2.2 of the main text. As for the non-

112   common coverage years 1980–1981 and 2012–2020, the weights for each year are

113   obtained by filtering all ET datasets covering that year for BMA analyses to obtain the

114   corresponding weights (see Figure S3). For example, there are a total of 27 ET datasets

115   covering the year 1980, and the weights obtained from the BMA analysis based on these

116   27 ET datasets are used as the weights of these 27 datasets in 1980; there are a total of

117   19 ET datasets covering the year 2019, and the weights obtained from the BMA analysis

118   based on these 19 ET datasets are used as the weights of these 19 datasets in 2019.

119

120   References

121   Ferreira, V. G., Montecino, H. D. C., Yakubu, C. I., and Heck, B.: Uncertainties of the
122   Gravity Recovery and Climate Experiment time-variable gravity-field solutions
123   based on three-cornered hat method, JARS, 10, 015015,
124   https://doi.org/10.1117/1.JRS.10.015015, 2016.

125   Foken, T., Wimmer, F., Mauder, M., Thomas, C., and Liebethal, C.: Some aspects of
126   the energy balance closure problem, Atmospheric Chemistry and Physics, 6,
127   4395–4402, https://doi.org/10.5194/acp-6-4395-2006, 2006.

128   Galindo, F. J. and Palacio, J.: Estimating the Instabilities of N Correlated Clocks, in:
129   Proceedings of the 31th Annual Precise Time and Time Interval Systems and
130   Applications Meeting, Proceedings of the 31th Annual Precise Time and Time
131   Interval Systems and Applications Meeting, 285–296, 1999.

132   Knauer, J., Zaehle, S., Medlyn, B. E., Reichstein, M., Williams, C. A., Migliavacca, M.,
133   De Kauwe, M. G., Werner, C., Keitel, C., Kolari, P., Limousin, J.-M., and
134   Linderson, M.-L.: Towards physiologically meaningful water-use efficiency
135   estimates from eddy covariance data, Global Change Biology, 24, 694–710,
136   https://doi.org/10.1111/gcb.13893, 2018.

137   Mahrt, L.: Stratified Atmospheric Boundary Layers, Boundary-Layer Meteorology, 90,
138   375–396, https://doi.org/10.1023/A:1001765727956, 1999.

139   McGloin, R., Šigut, L., Fischer, M., Foltýnová, L., Chawla, S., Trnka, M., Pavelka, M.,
140   and Marek, M. V.: Available Energy Partitioning During Drought at Two Norway
141   Spruce Forests and a European Beech Forest in Central Europe, Journal of
142   Geophysical Research: Atmospheres, 124, 3726–3742,
143   https://doi.org/10.1029/2018JD029490, 2019.

144   Medlyn, B. E., De Kauwe, M. G., Lin, Y.-S., Knauer, J., Duursma, R. A., Williams, C.
145   A., Arneth, A., Clement, R., Isaac, P., Limousin, J.-M., Linderson, M.-L., Meir, P.,
146   Martin-StPaul, N., and Wingate, L.: How do leaf and ecosystem measures of
147   water-use efficiency compare?, New Phytologist, 216, 758–770,
148   https://doi.org/10.1111/nph.14626, 2017.

149   Pastorello, G., Trotta, C., Canfora, E., Chu, H., Christianson, D., Cheah, Y.-W.,
150   Poindexter, C., Chen, J., Elbashandy, A., Humphrey, M., Isaac, P., Polidori, D.,
151   Reichstein, M., Ribeca, A., van Ingen, C., Vuichard, N., Zhang, L., Amiro, B.,
152   Ammann, C., Arain, M. A., Ardö, J., Arkebauer, T., Arndt, S. K., Arriga, N.,
153   Aubinet, M., Aurela, M., Baldocchi, D., Barr, A., Beamesderfer, E., Marchesini, L.

B., Bergeron, O., Beringer, J., Bernhofer, C., Berveiller, D., Billesbach, D., Black, T. A., Blanken, P. D., Bohrer, G., Boike, J., Bolstad, P. V., Bonal, D., Bonnefond, J.-M., Bowling, D. R., Bracho, R., Brodeur, J., Brümmer, C., Buchmann, N., Burban, B., Burns, S. P., Buysse, P., Cale, P., Cavagna, M., Cellier, P., Chen, S., Chini, I., Christensen, T. R., Cleverly, J., Collalti, A., Consalvo, C., Cook, B. D., Cook, D., Coursolle, C., Cremonese, E., Curtis, P. S., D'Andrea, E., da Rocha, H., Dai, X., Davis, K. J., Cinti, B. D., Grandcourt, A. de, Ligne, A. D., De Oliveira, R. C., Delpierre, N., Desai, A. R., Di Bella, C. M., Tommasi, P. di, Dolman, H., Domingo, F., Dong, G., Dore, S., Duce, P., Dufrêne, E., Dunn, A., Dušek, J., Eamus, D., Eichelmann, U., ElKhidir, H. A. M., Eugster, W., Ewenz, C. M., Ewers, B., Famulari, D., Fares, S., Feigenwinter, I., Feitz, A., Fensholt, R., Filippa, G., Fischer, M., Frank, J., Galvagno, M., et al.: The FLUXNET2015 dataset and the ONEFlux processing pipeline for eddy covariance data, Sci Data, 7, 225, https://doi.org/10.1038/s41597-020-0534-3, 2020.

Senay, G. B., Leake, S., Nagler, P. L., Artan, G., Dickinson, J., Cordova, J. T., and Glenn, E. P.: Estimating basin scale evapotranspiration (ET) by water balance and remote sensing methods, Hydrological Processes, 25, 4037–4049, https://doi.org/10.1002/hyp.8379, 2011.

Tapley, B. D., Watkins, M. M., Flechtner, F., Reigber, C., Bettadpur, S., Rodell, M., Sasgen, I., Famiglietti, J. S., Landerer, F. W., Chambers, D. P., Reager, J. T., Gardner, A. S., Save, H., Ivins, E. R., Swenson, S. C., Boening, C., Dahle, C., Wiese, D. N., Dobslaw, H., Tamisiea, M. E., and Velicogna, I.: Contributions of GRACE to understanding climate change, Nat. Clim. Chang., 9, 358–369, https://doi.org/10.1038/s41558-019-0456-2, 2019.

Vrugt, J. A., Diks, C. G. H., and Clark, M. P.: Ensemble Bayesian model averaging using Markov Chain Monte Carlo sampling, Environ Fluid Mech, 8, 579–595, https://doi.org/10.1007/s10652-008-9106-3, 2008.

Xu, T., Guo, Z., Xia, Y., Ferreira, V. G., Liu, S., Wang, K., Yao, Y., Zhang, X., and Zhao, C.: Evaluation of twelve evapotranspiration products from machine learning, remote sensing and land surface models over conterminous United States, Journal of Hydrology, 578, 124105, https://doi.org/10.1016/j.jhydrol.2019.124105, 2019.

Yuan, K., Zhu, Q., Zheng, S., Zhao, L., Chen, M., Riley, W. J., Cai, X., Ma, H., Li, F., Wu, H., and Chen, L.: Deforestation reshapes land-surface energy-flux partitioning, Environ. Res. Lett., 16, 024014, https://doi.org/10.1088/1748-

188   9326/abd8f9, 2021.

189   Zhang, K., Kimball, J. S., Nemani, R. R., and Running, S. W.: A continuous satellite-

190   derived global record of land surface evapotranspiration from 1983 to 2006, Water

191   Resources Research, 46, https://doi.org/10.1029/2009WR008800, 2010.

192   Zhu, G., Zhang, K., Li, X., Liu, S.-M., Ding, Z.-Y., Ma, J.-Z., Huang, C.-L., Han, T.,

193   and He, J.-H.: Evaluating the complementary relationship for estimating

194   evapotranspiration using the multi-site data across north China, Agricultural and

195   Forest   Meteorology,   230–231,   33–44,
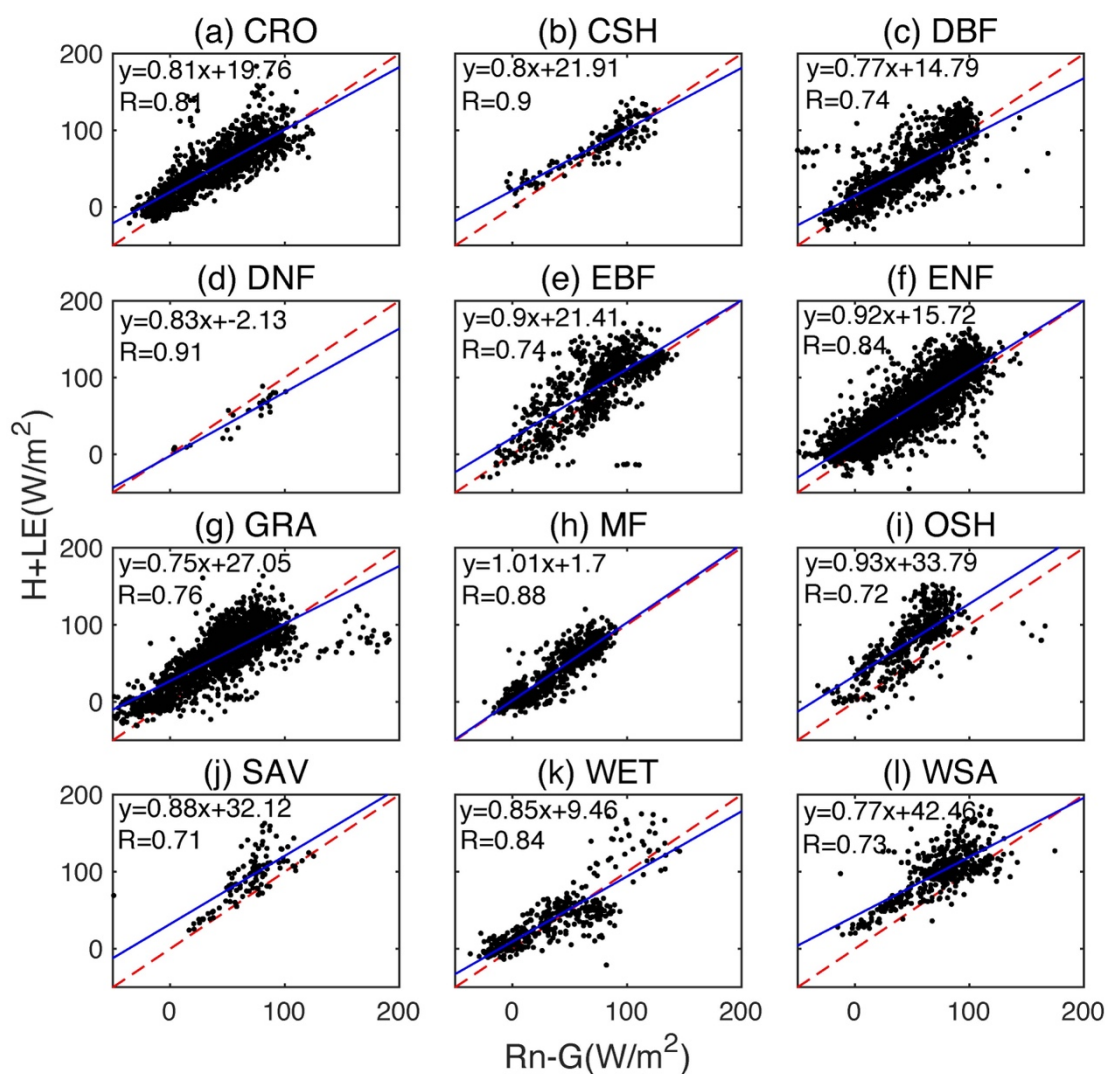
196   https://doi.org/10.1016/j.agrformet.2016.06.006, 2016.

197

198
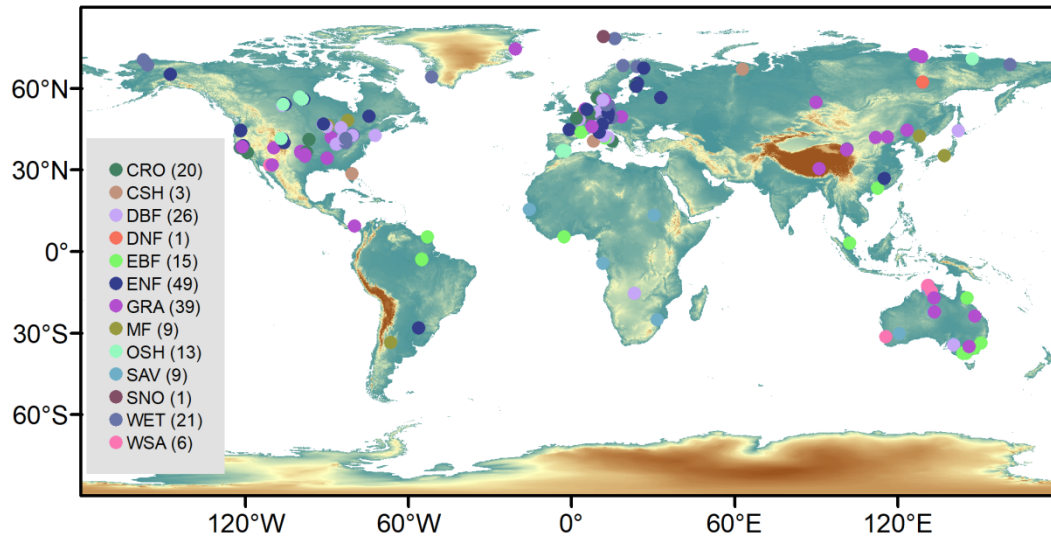
Fig. S1: Global spatial distribution of the 212 ET from FLUXNET and their corresponding vegetation types. Numbers in parentheses indicate the number of sites for each vegetation type (identified in Table S2).

9

204

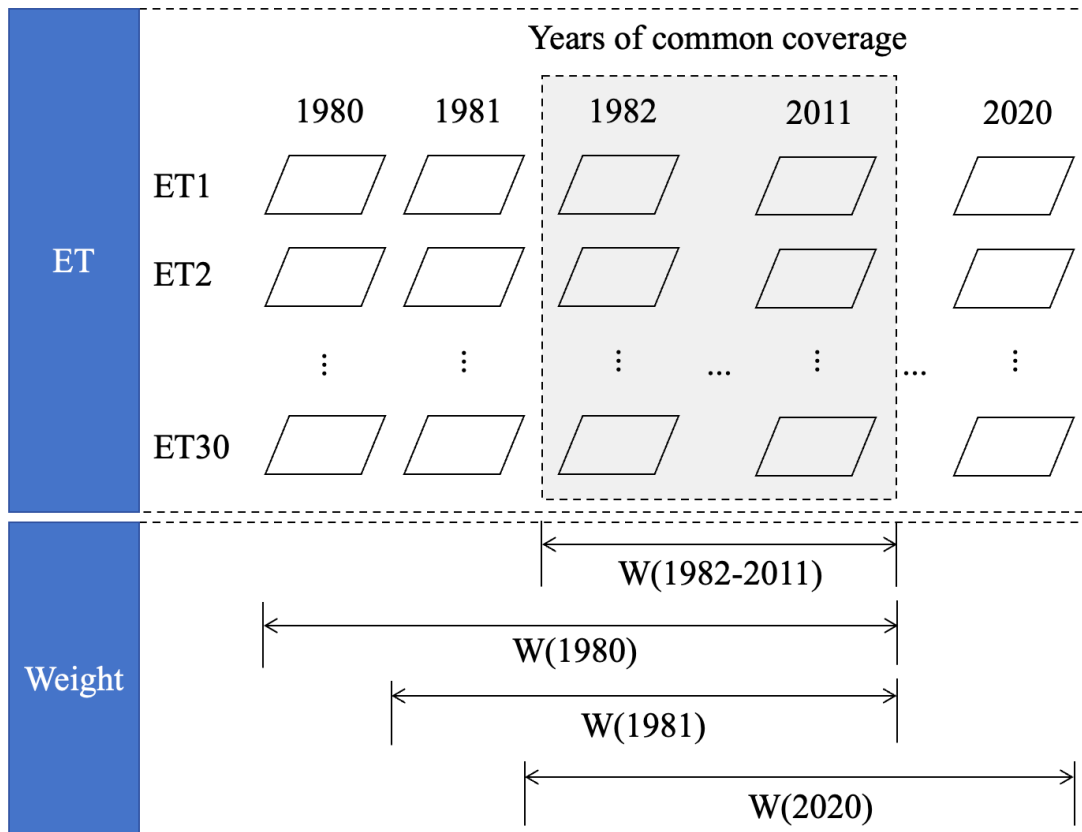**Fig. S2**: Least-squares linear-regression-based energy balance closed scatter fit for monthly-scale flux tower data.
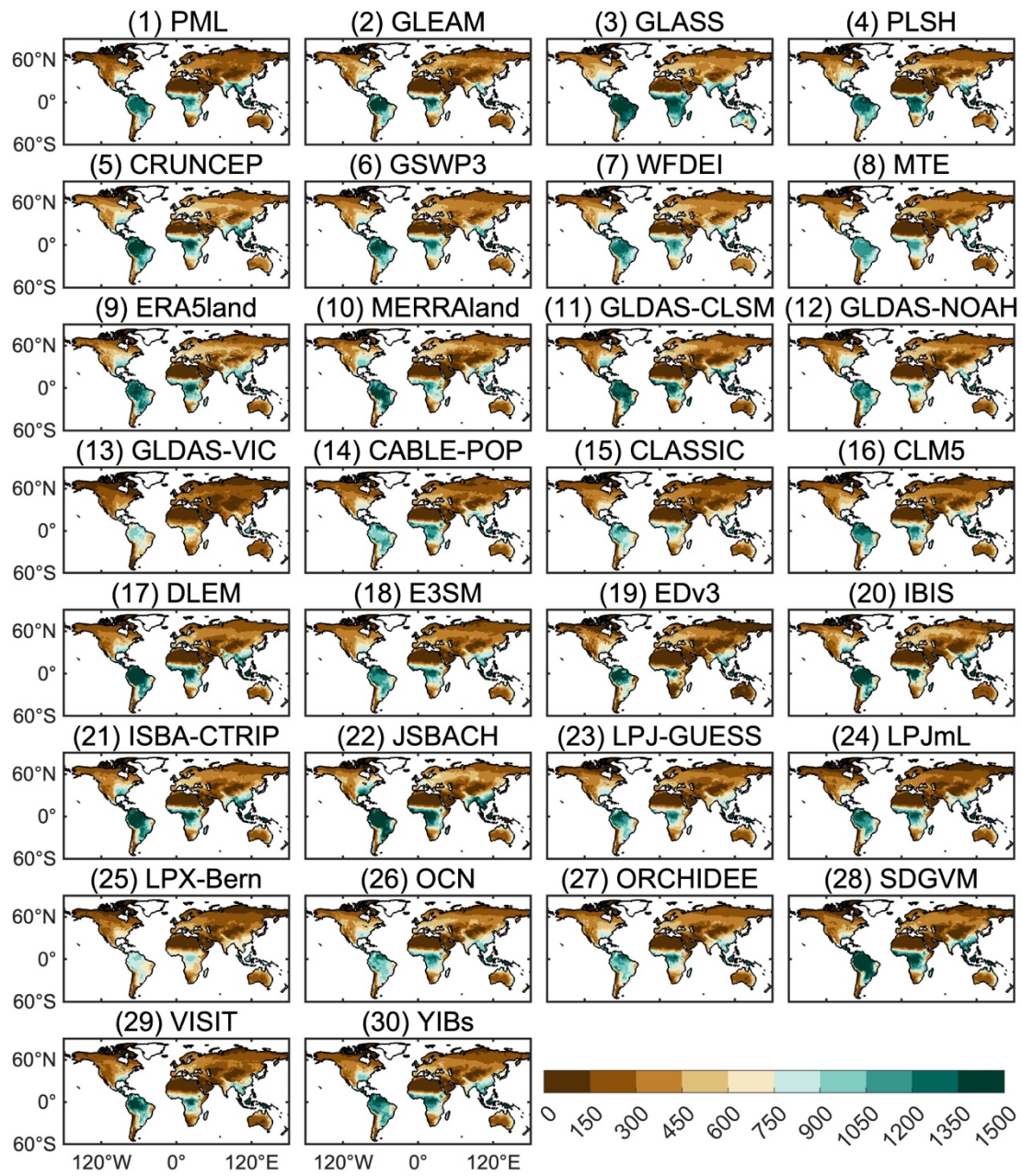
208

209

210

Fig. S3: Weighting scheme for ET datasets during non-common coverage years.
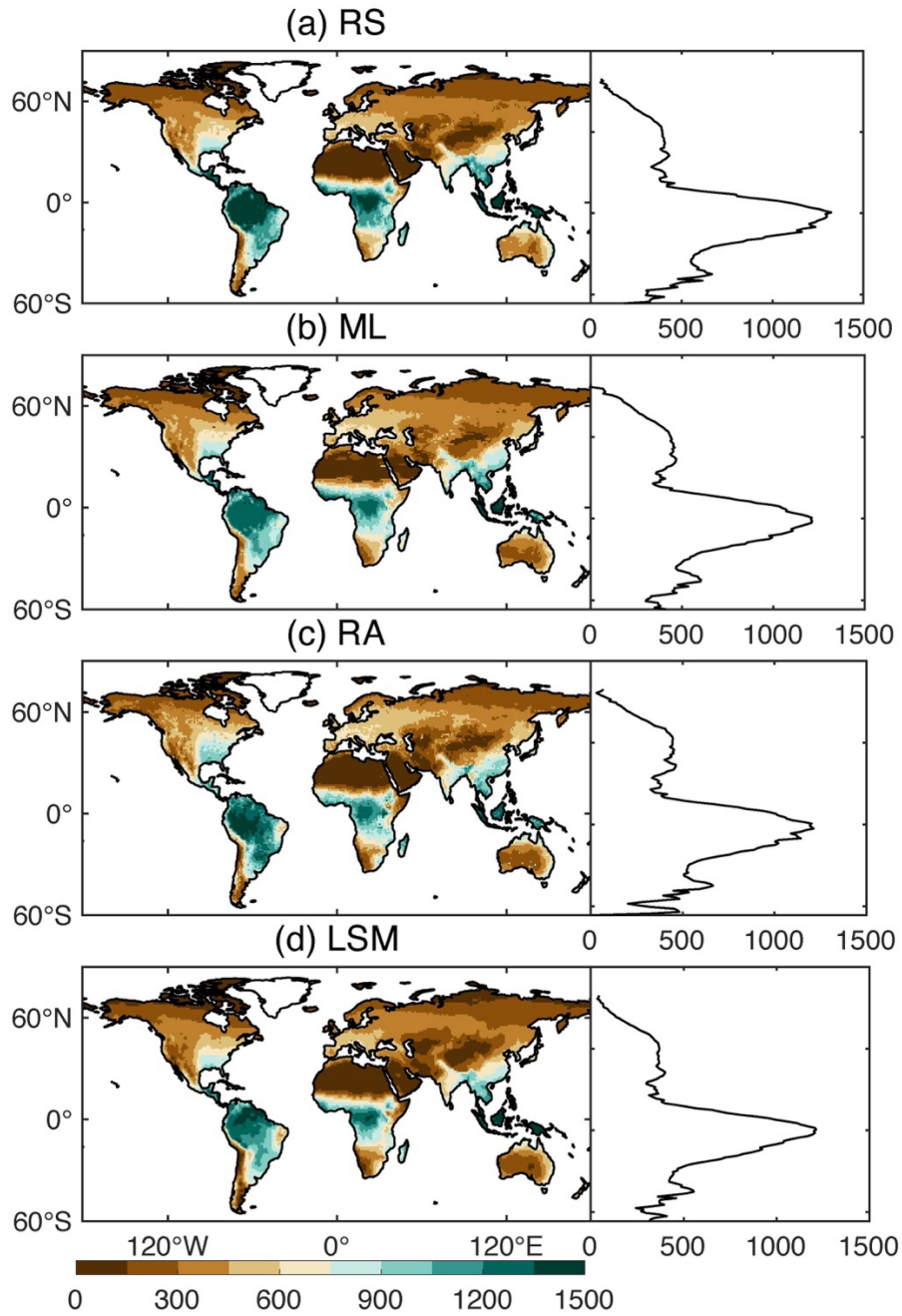
213

214

215

Fig. S4: Multi-year average evapotranspiration during 1982–2011 (unit: mm).

217

Fig. S5: Multi-year average evapotranspiration of multi-dataset median for four types of evapotranspiration datasets during 1982–2011 (unit: mm).
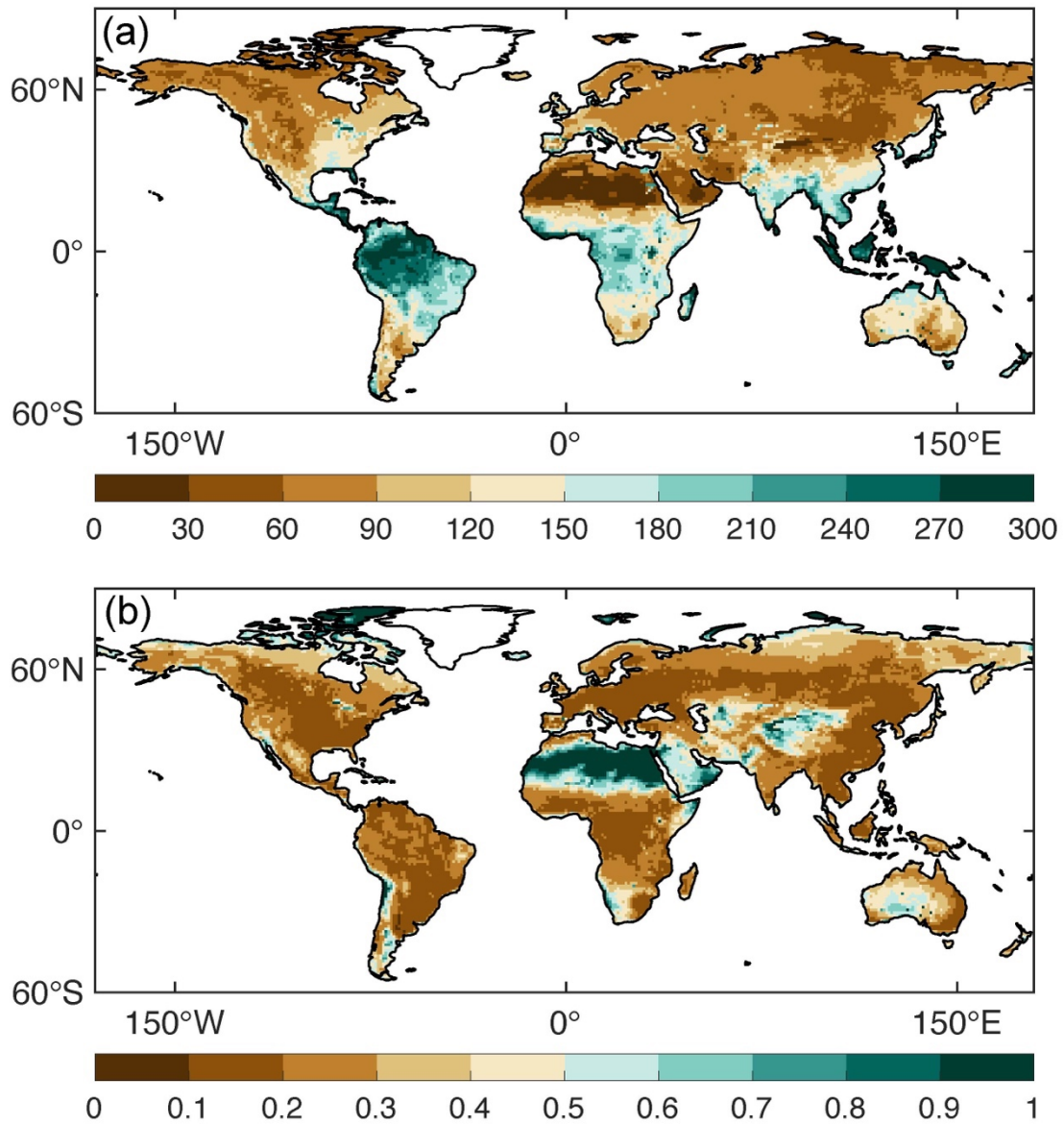
Fig. S6: (a) Standard deviation (STD) and (b) standardized standard deviation of 30 ET datasets at the multi-year average scale (unit: mm).

226
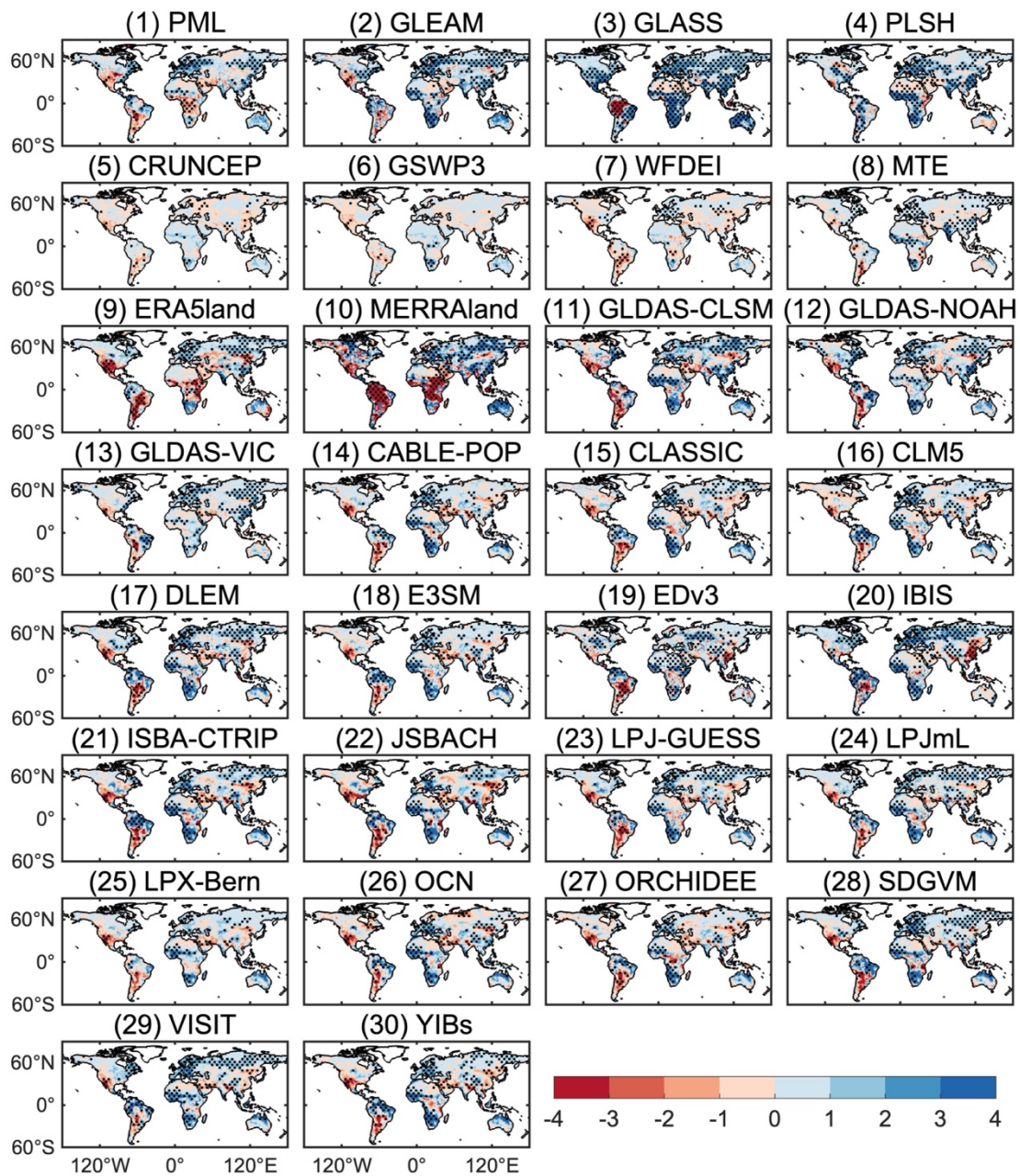
Fig. S7: Interannual trends in evapotranspiration datasets during 1982–2011 (unit: mm·yr^{-1}) (the black dotted areas indicate that the trend in these grid points was significant at the 95% level).

227

228

229

230

231
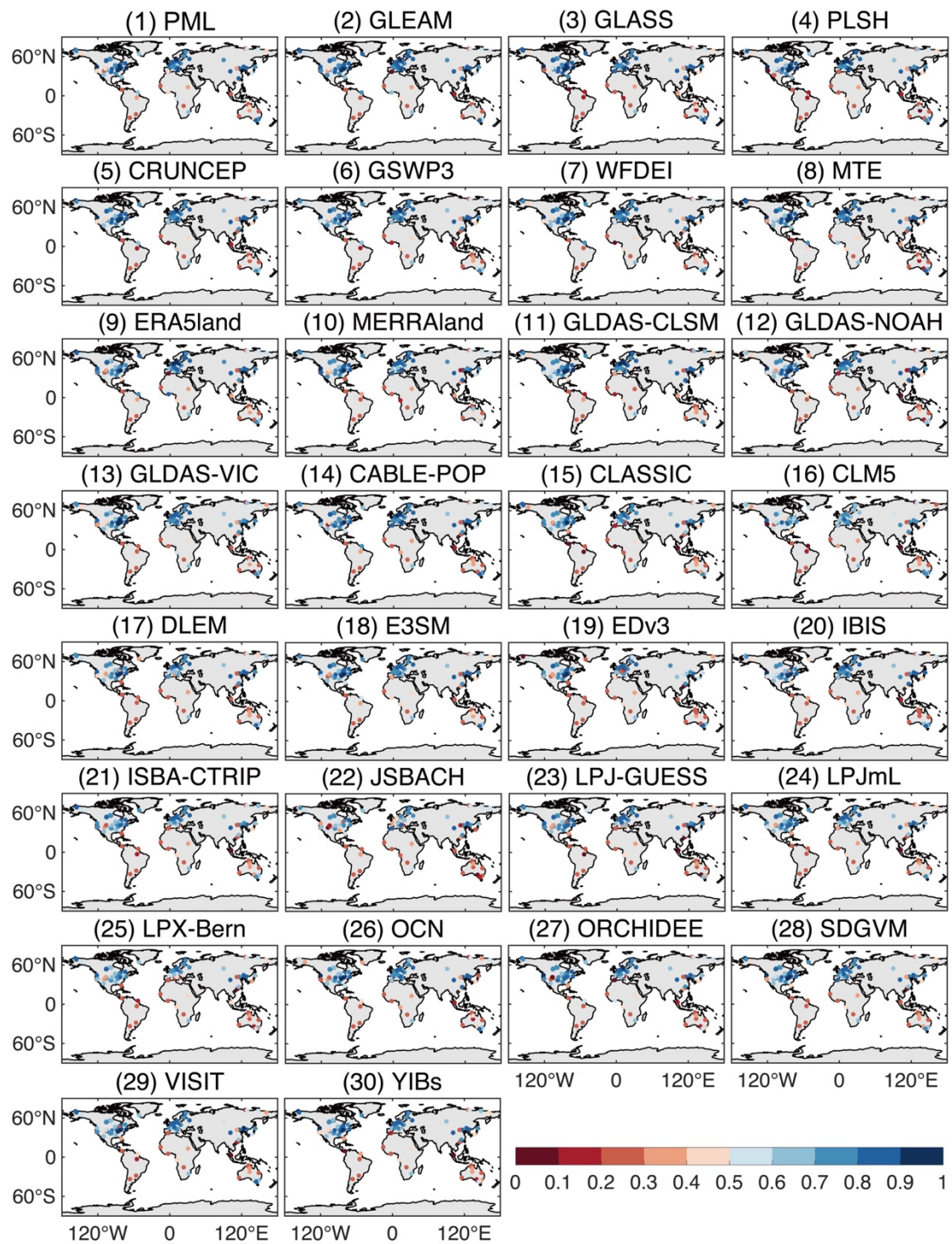
Fig. S8: Spatial distribution of correlation coefficients (R) for site validation of each ET dataset during 1991–2011.

237
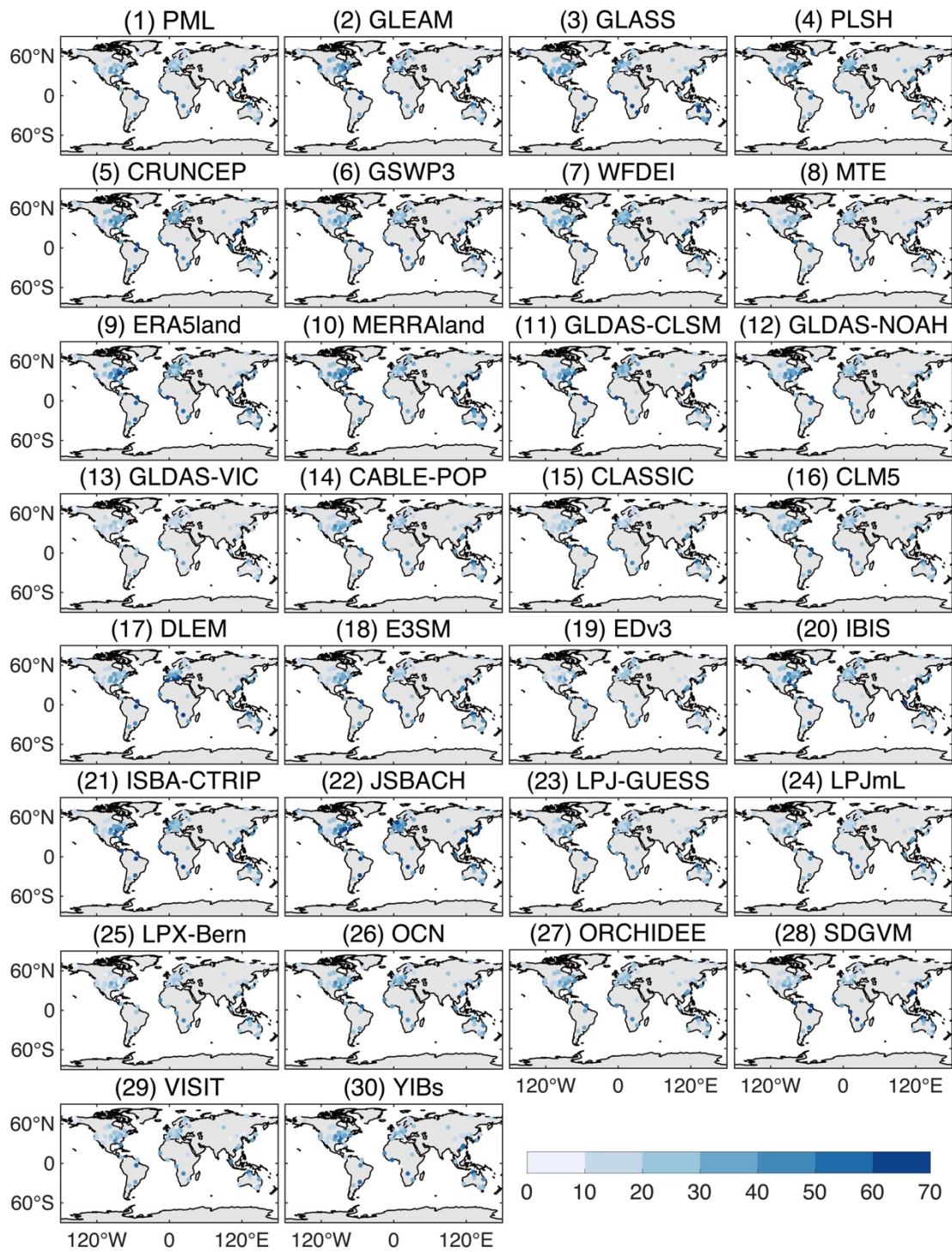
Fig. S9: Spatial distribution of mean absolute errors (MAE) for site validation of each
ET dataset during 1991–2011.

241

242
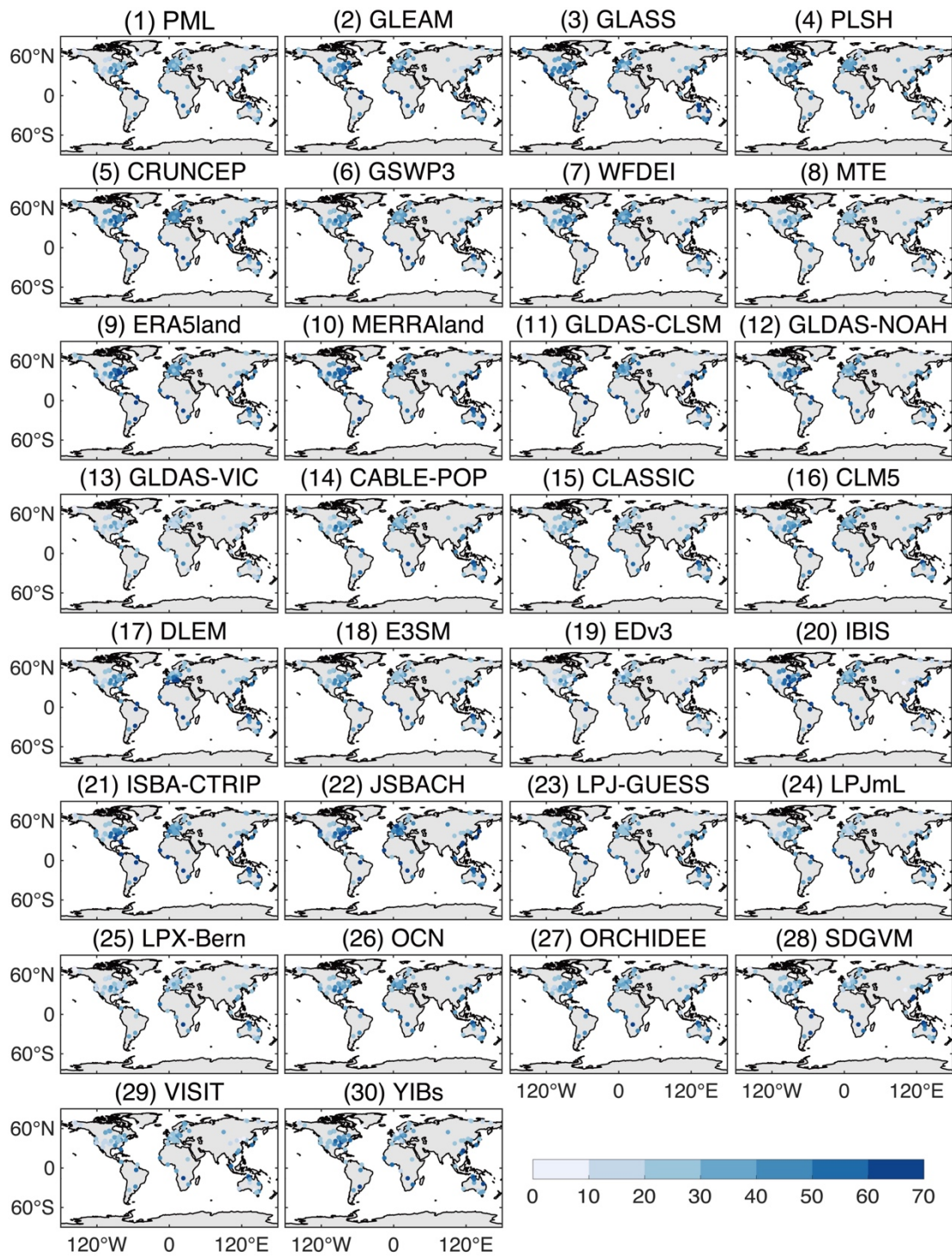
Fig. S10: Spatial distribution of root-mean-square errors (RMSE) for site validation of each ET dataset during 1991–2011.

243

244

245

246

247

248

249
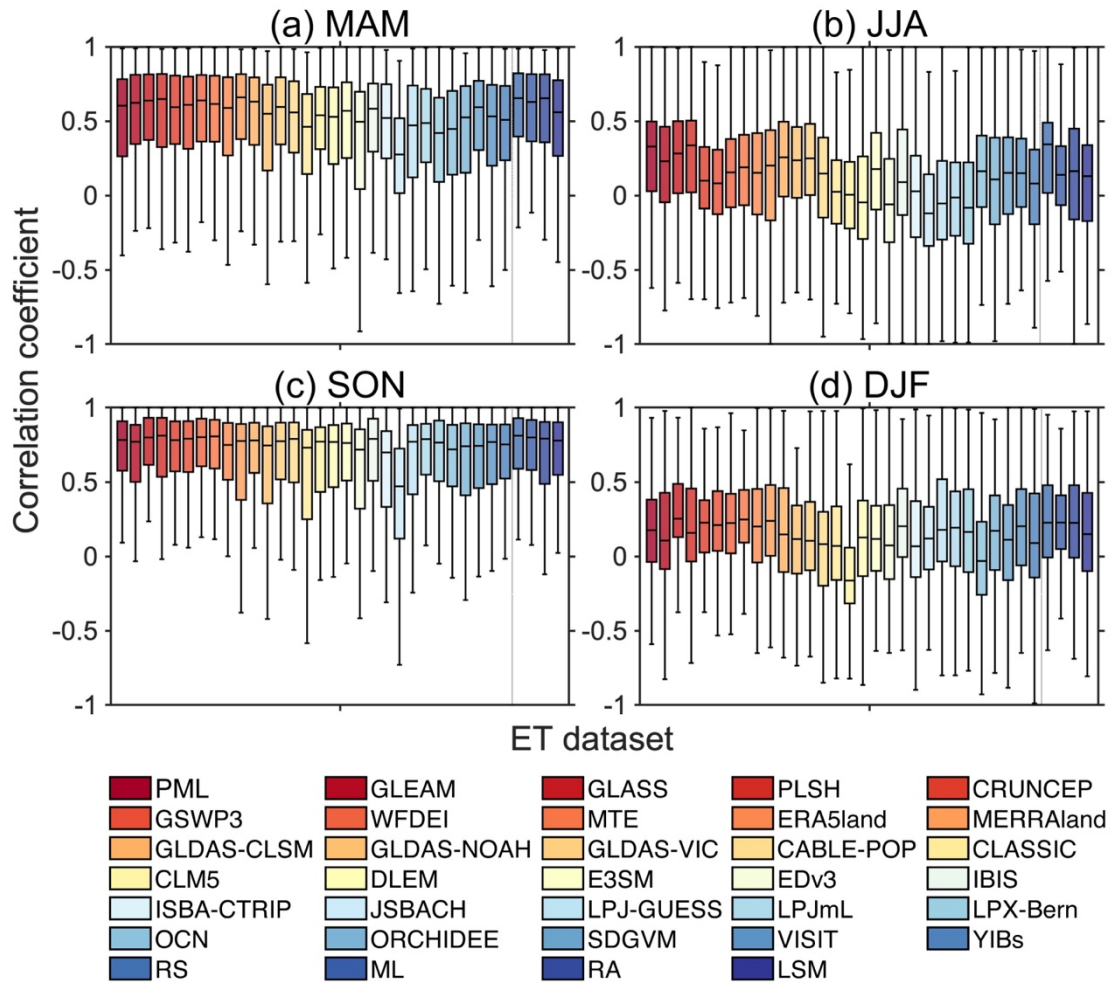
Fig. S11: Spatial distribution of seasonal correlation coefficients (R), validated at each ET dataset site, 1991–2011. Each box-and-whisker plot represents the range of uncertainty across sites for that scenario (for each box, the central horizontal line represents the median of the sample, the upper and lower boundaries represent the 75th and 25th percentile values, respectively, and the two 'whiskers' extend to the maximum and minimum values that are not considered outliers, which are plotted separately).

256

257
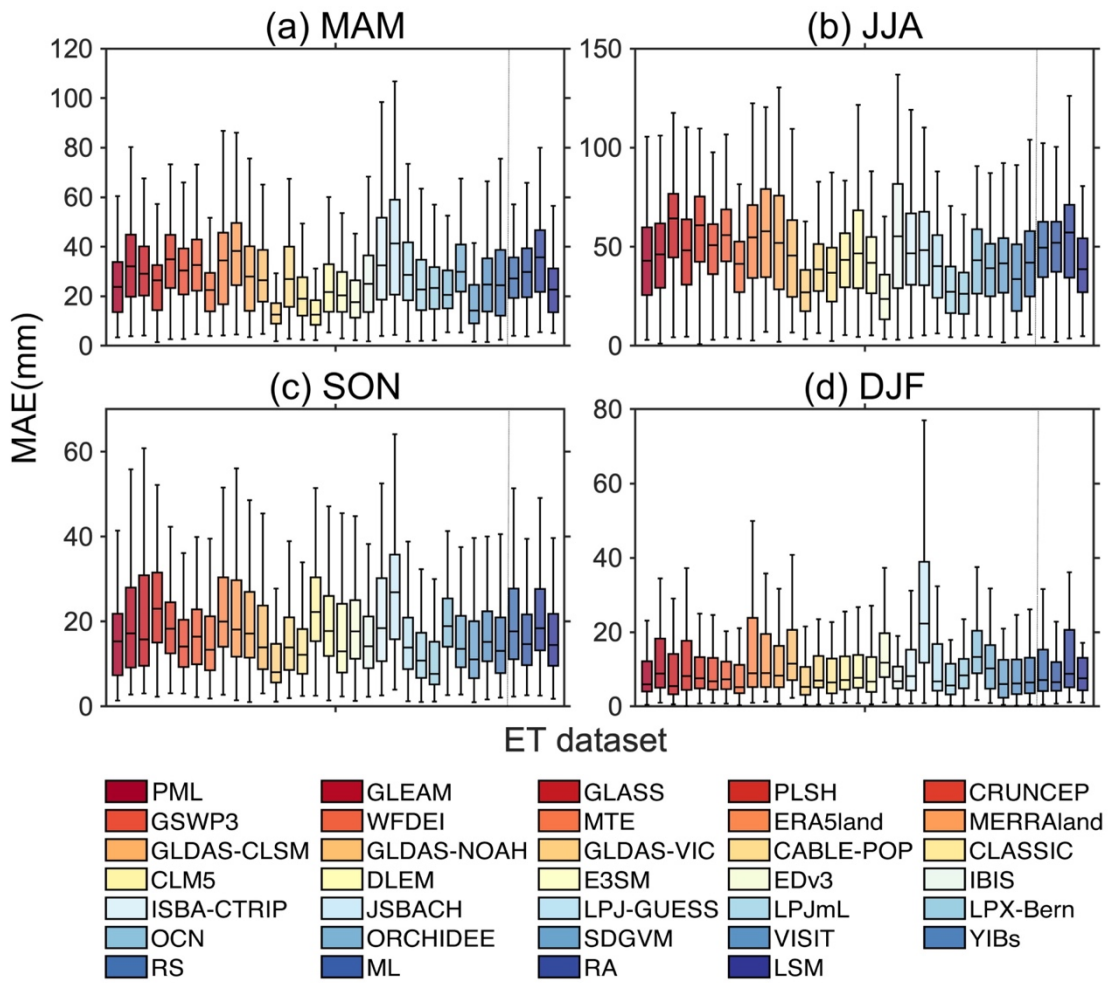
Fig. S12: Spatial distribution of seasonal mean absolute errors (MAE) in the validation of each ET dataset site, 1991–2011. Each box-and-whisker plot represents the range of uncertainty across sites for that scenario (for each box, the central horizontal line represents the median of the sample, the upper and lower boundaries represent the 75th and 25th percentile values, respectively, and the two 'whiskers' extend to the maximum and minimum values that are not considered outliers, which are plotted separately).

268

269

Fig. S13: Spatial distribution of seasonal root-mean-square errors (RMSE) validated at each ET dataset site for 1991–2011. Each box-and-whisker plot represents the range of uncertainty across sites for that scenario (for each box, the central horizontal line represents the median of the sample, the upper and lower boundaries represent the 75th and 25th percentile values, respectively, and the two 'whiskers' extend to the maximum and minimum values that are not considered outliers, which are plotted separately).

276

277

278

Fig. S14: Correlation coefficients (R) between each ET dataset and ET from FLUXNET for different vegetation types, 1991–2011. Each box-and-whisker plot indicates the range of uncertainty for the different sites in the scenario (for each box, the central horizontal line indicates the median of the sample, its upper and lower boundaries indicate the 75th and 25th percentile values, respectively, and the two 'whiskers' extend to the maximum and minimum values that are not considered outliers, and outliers are plotted separately)

286

287
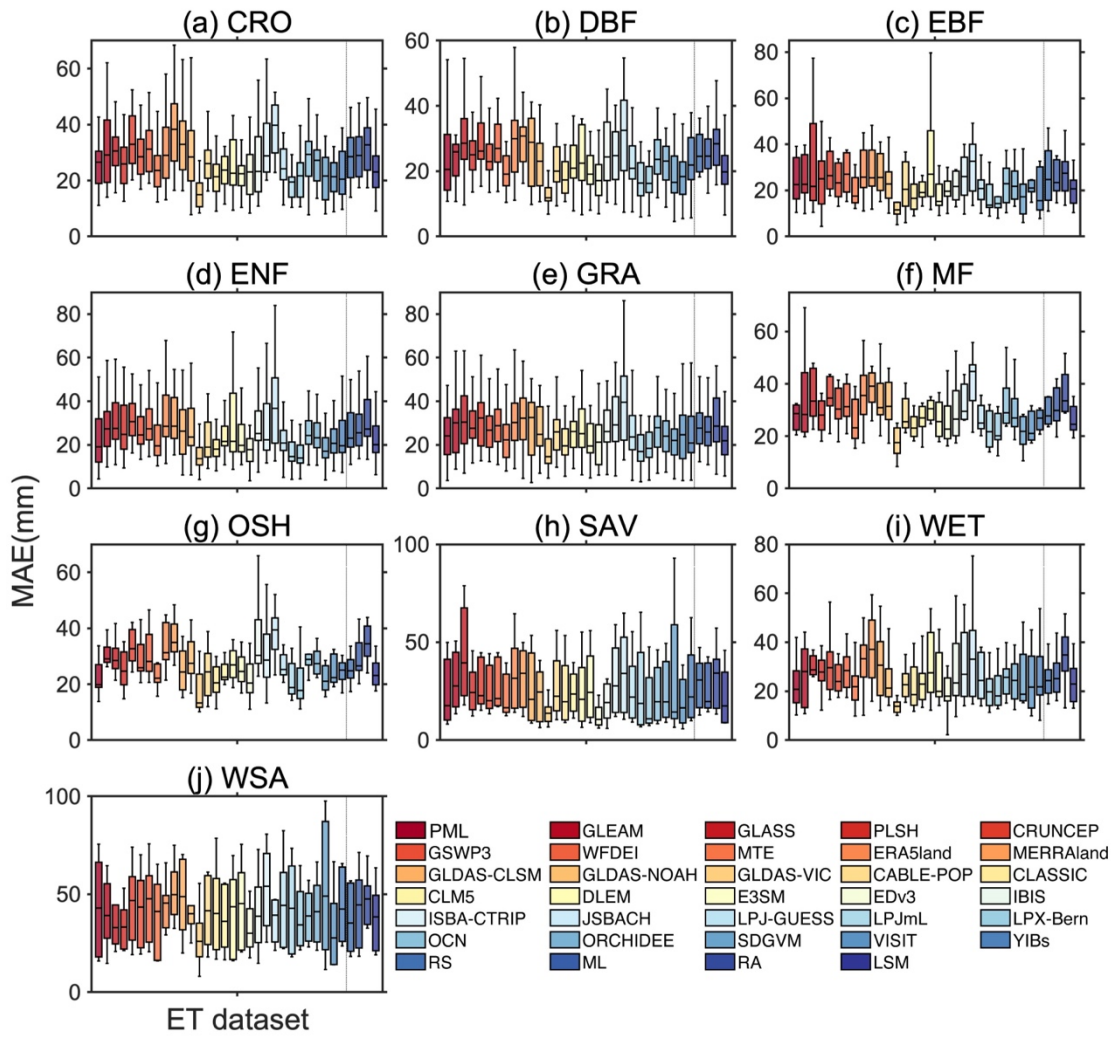
Fig. S15: Mean absolute errors (MAE) for each ET dataset and ET from FLUXNET across vegetation types, 1991–2011. Each box-and-whisker plot represents the range of uncertainty for the different sites in the scenario (for each box, the central horizontal line represents the median of the sample, the upper and lower borders represent the 75th and 25th percentile values, respectively, and the two 'whiskers' extend to the maximum and minimum values that are not considered outliers, which are plotted separately).
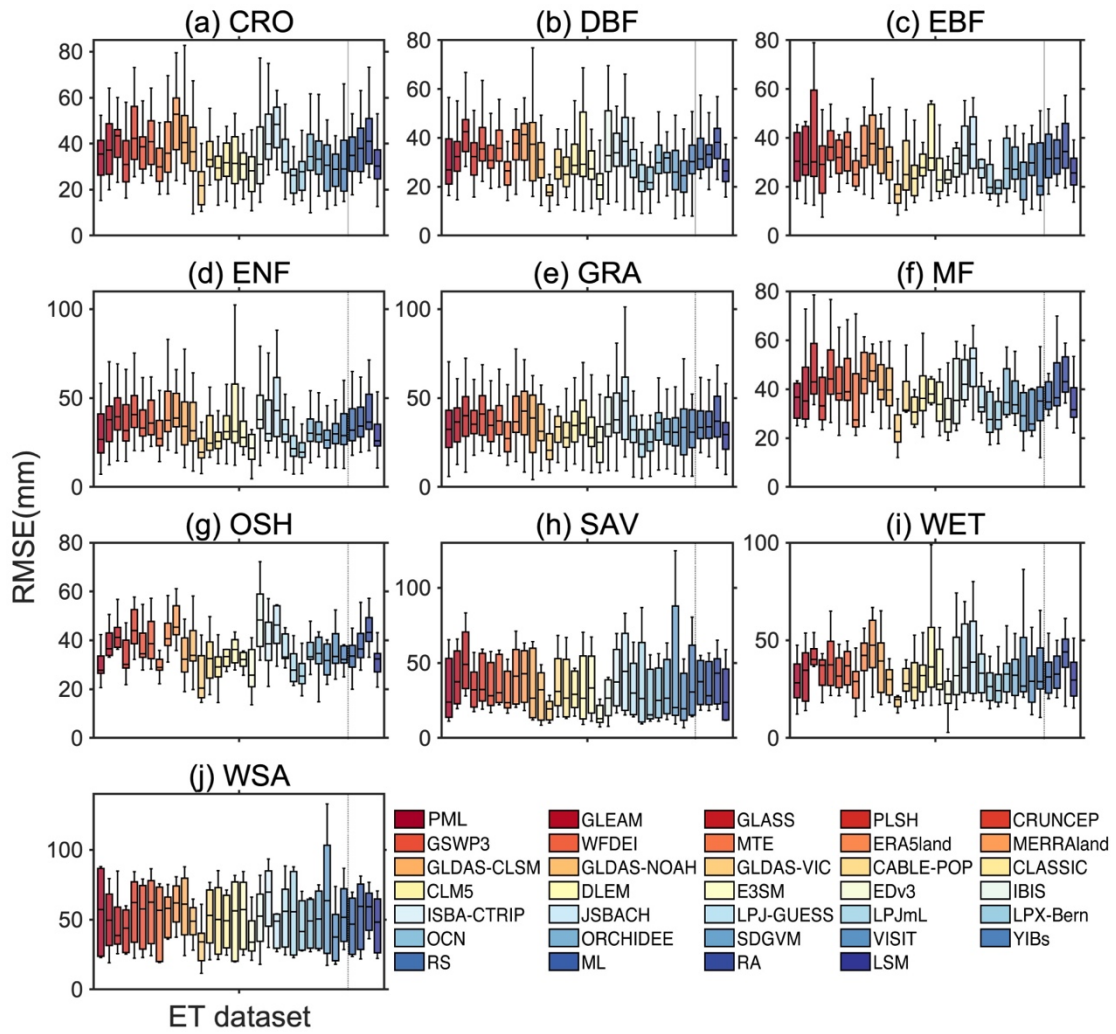
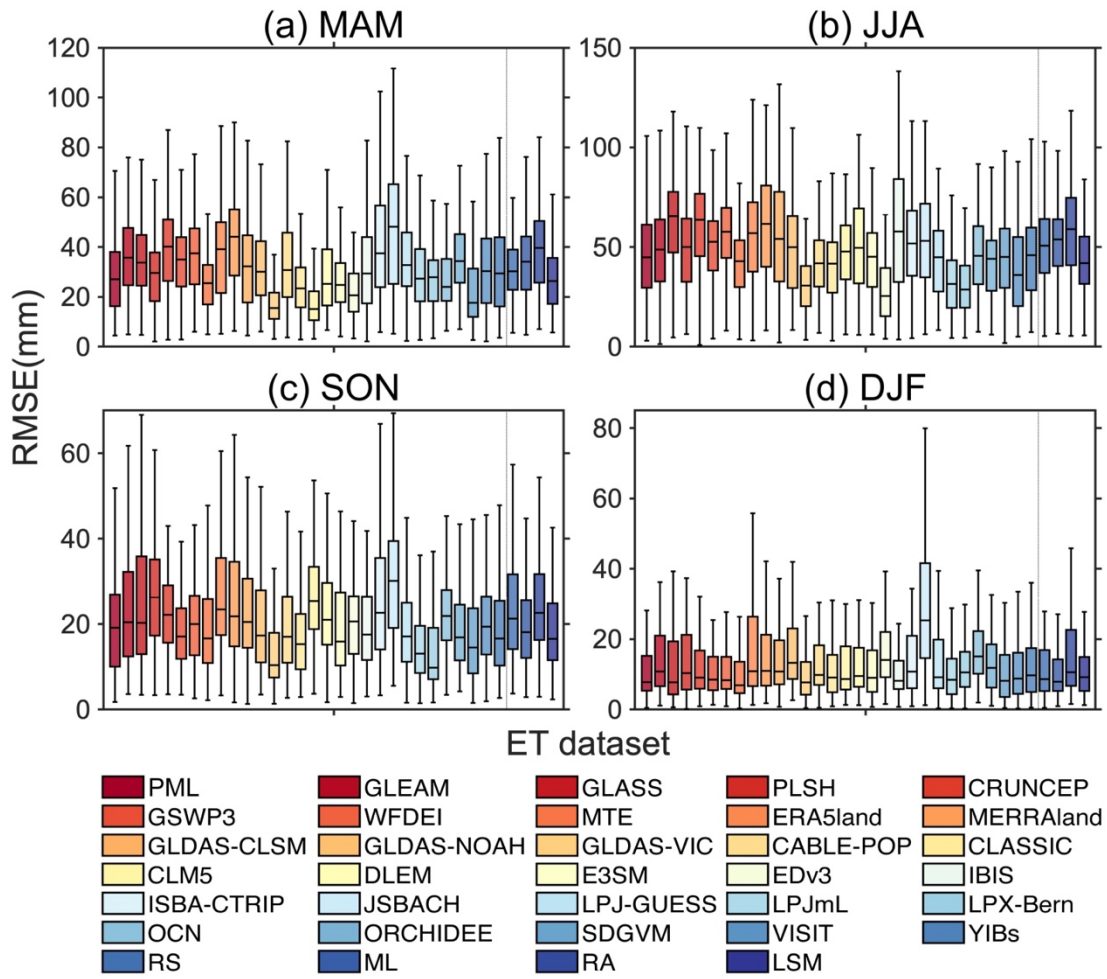**Fig. S16**: Root-mean-square errors (RMSE) for each ET dataset and ET from FLUXNET for different vegetation types, 1991–2011. Each box-and-whisker plot represents the range of uncertainty for the different sites in the scenario (for each box, the central horizontal line represents the median of the sample, the upper and lower boundaries represent the 75th and 25th percentile values, respectively, and the two 'whiskers' extend to the maximum and minimum values that are not considered outliers, which are plotted separately).
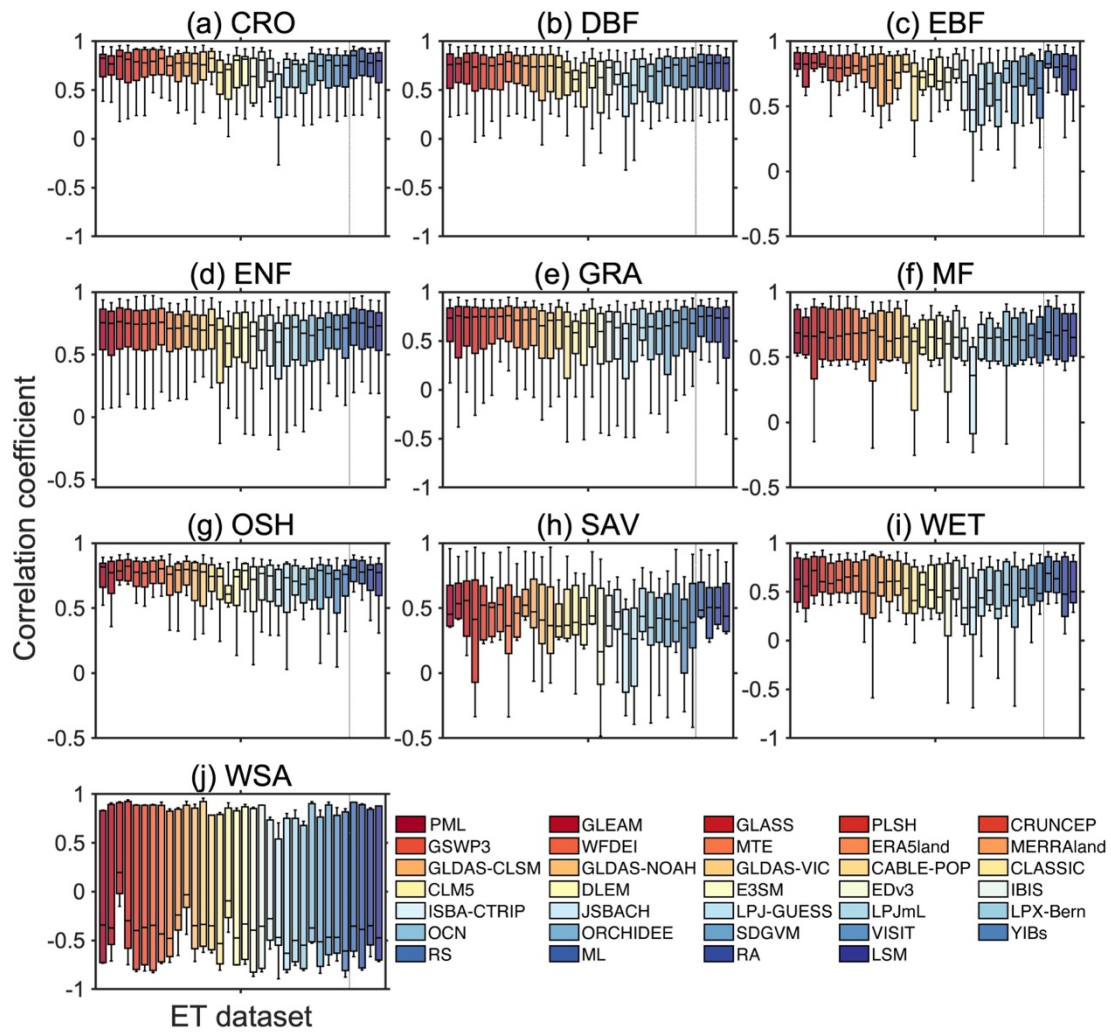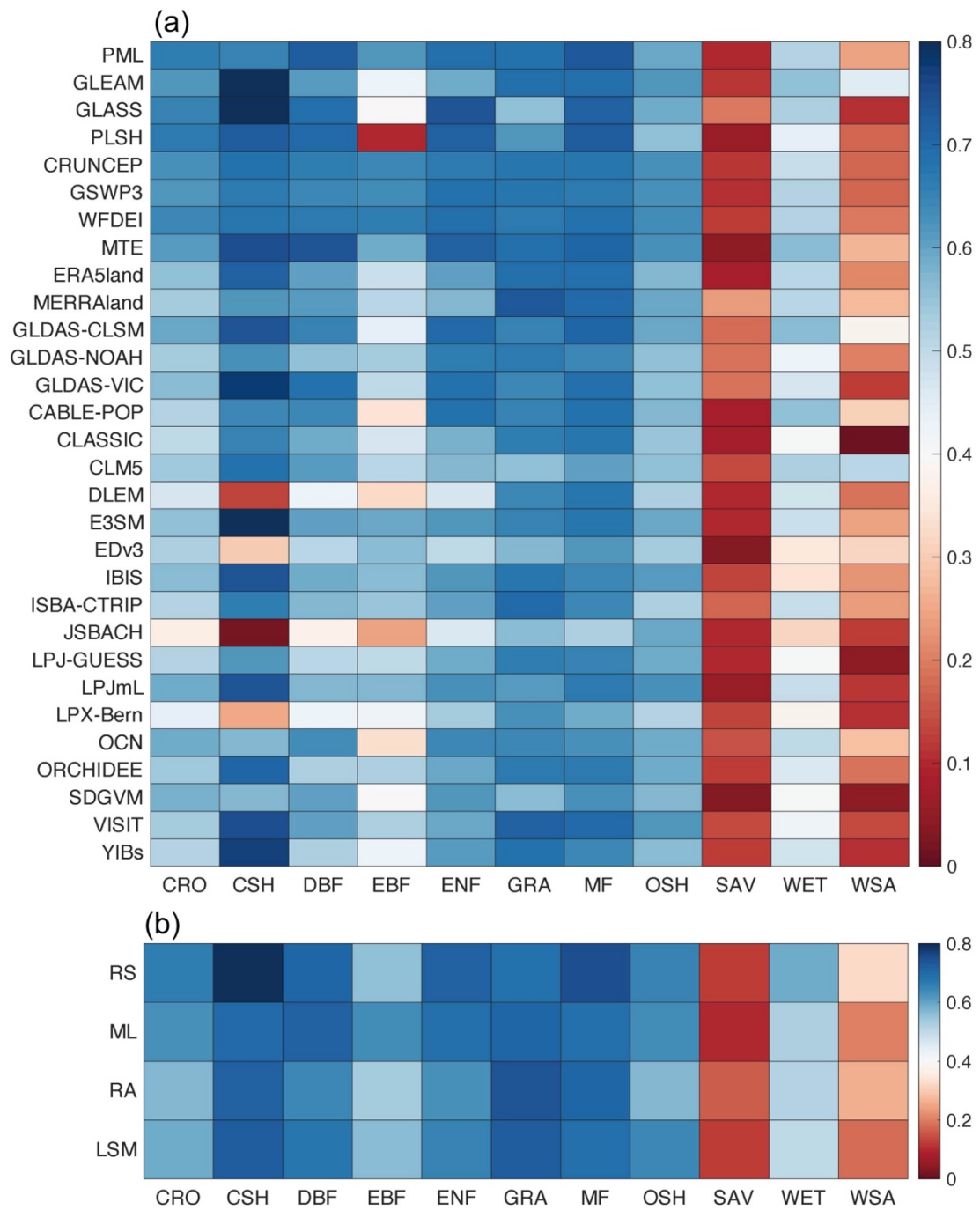
Fig. S17: Correlation coefficients between monthly values of ET datasets and ET from FLUXNET for 12 vegetation types during 1991–2011.
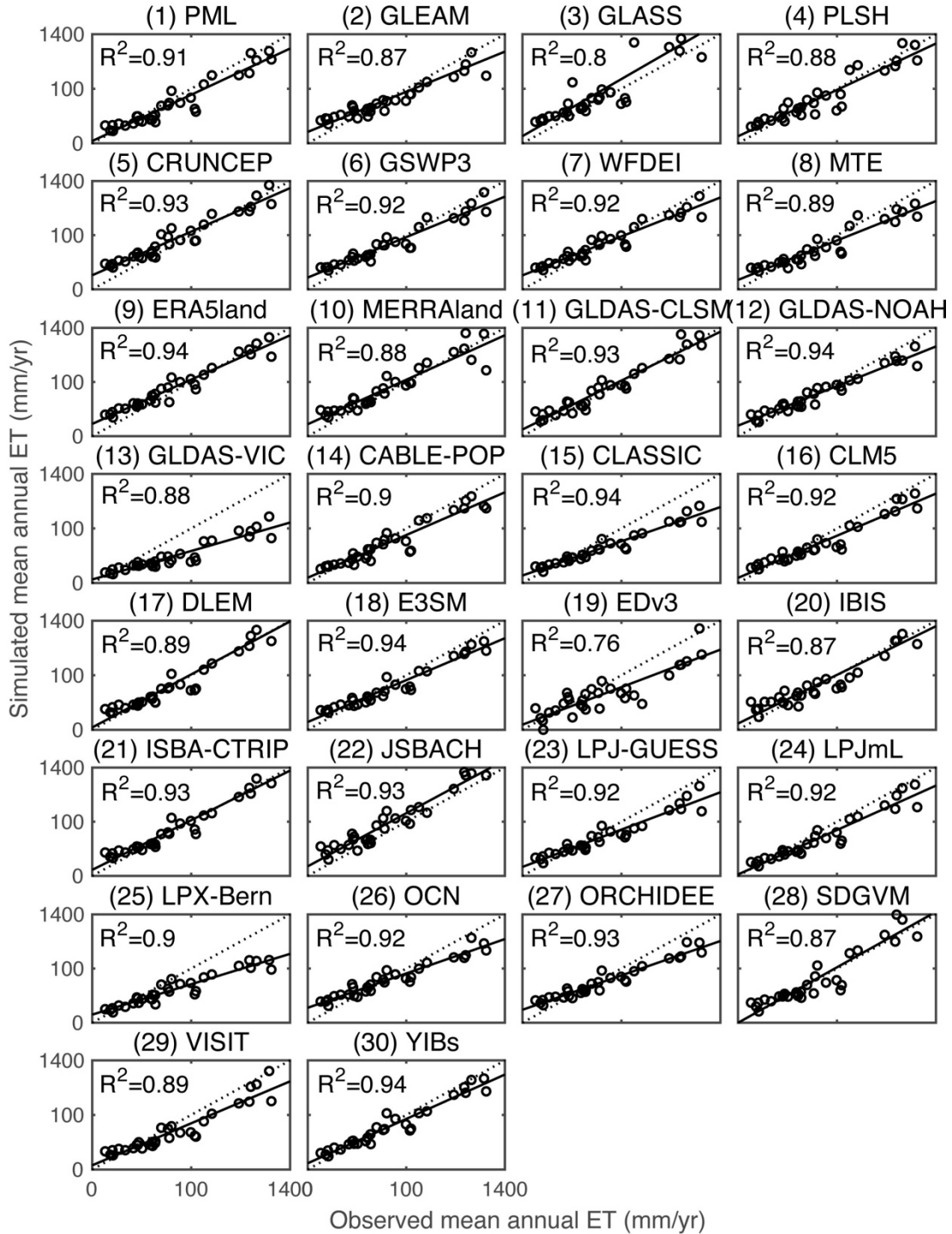
Fig. S18: Comparison of multi-year average evapotranspiration from 30 ET datasets and multi-year average observed evapotranspiration from basin water balance.

317
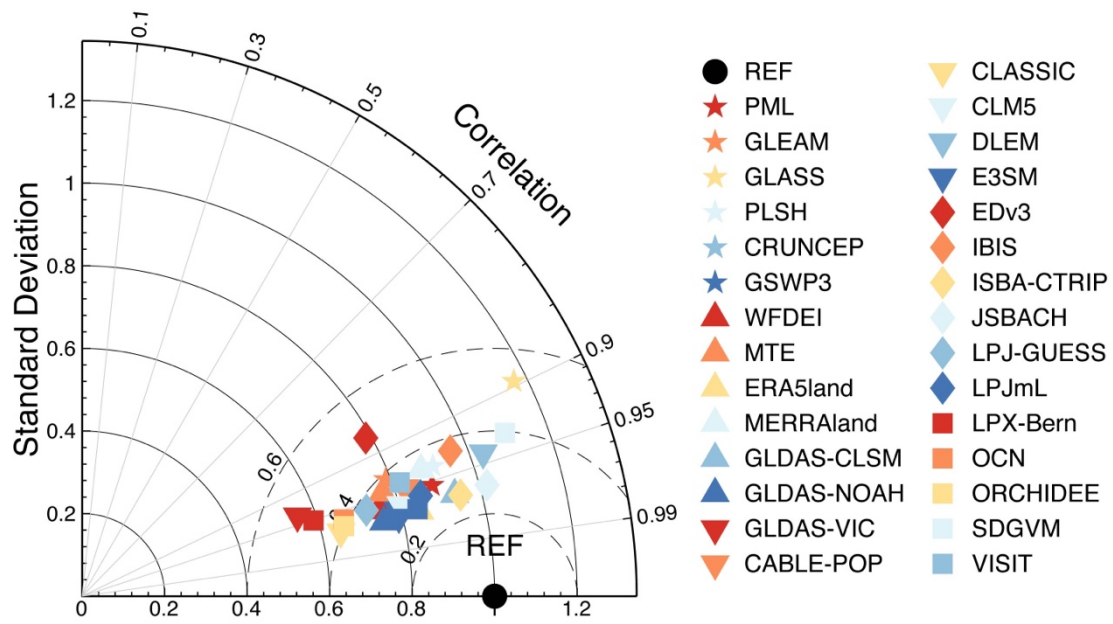
Fig. S19: Overall accuracy of simulated basin-scale evapotranspiration for all ET datasets.

318

319

320
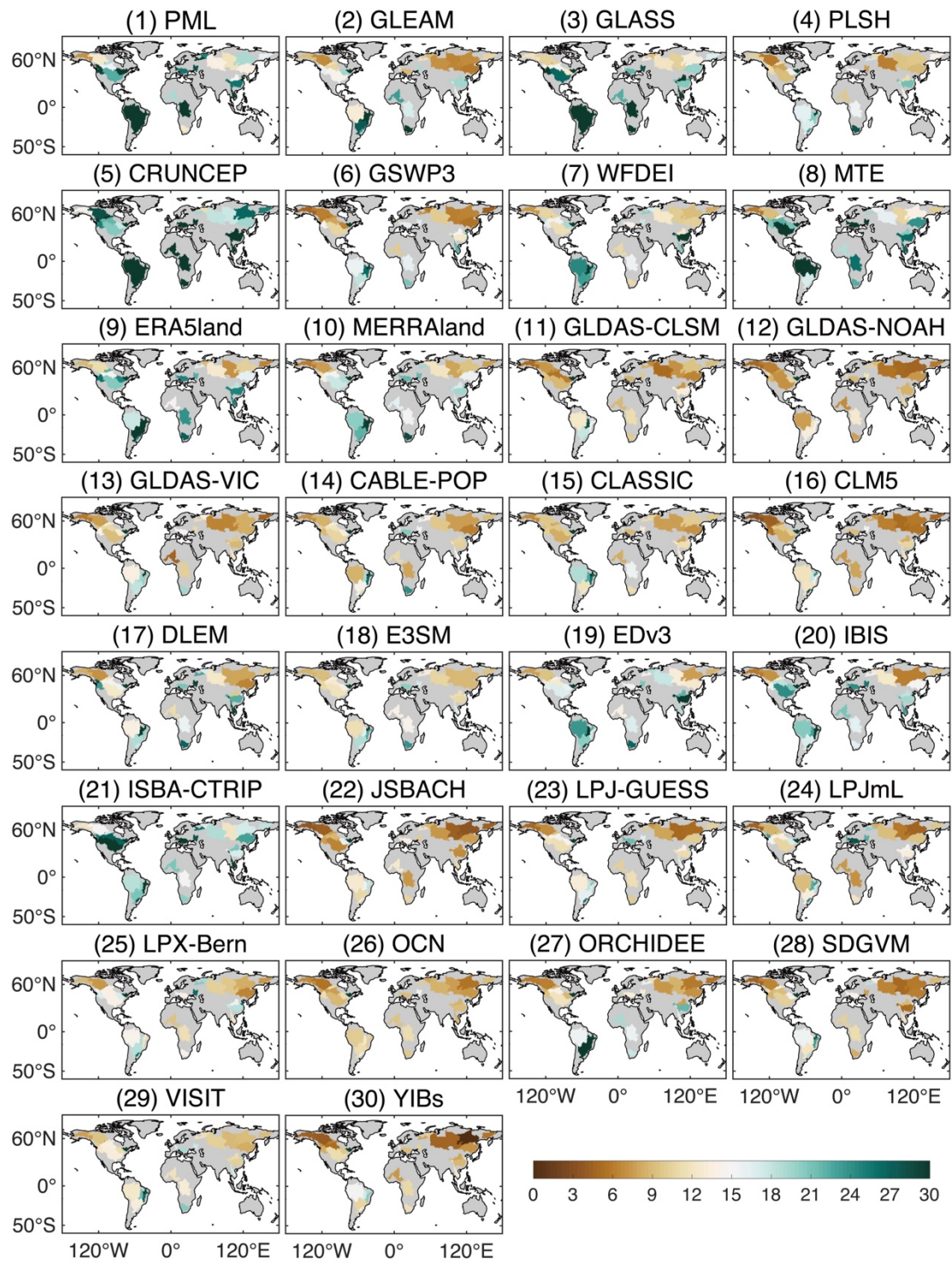
Fig. S20: Spatial distribution of TCH uncertainty for 32 basins globally during 1982–2011 (unit: mm).
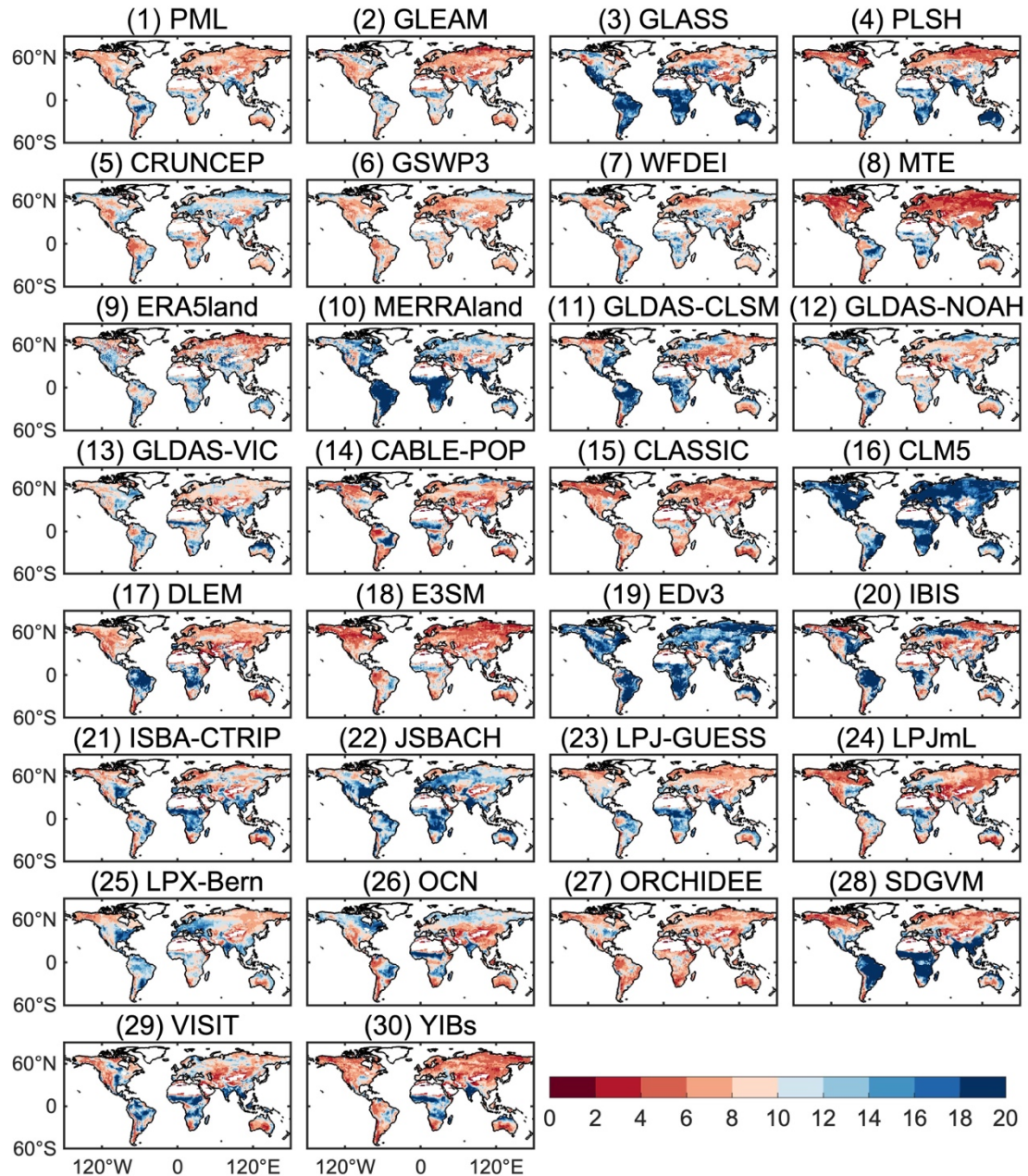
Fig. S21: Spatial distribution of uncertainty of TCH for each ET dataset on monthly scale for the common coverage years from 1982 to 2011 (unit: mm).

329
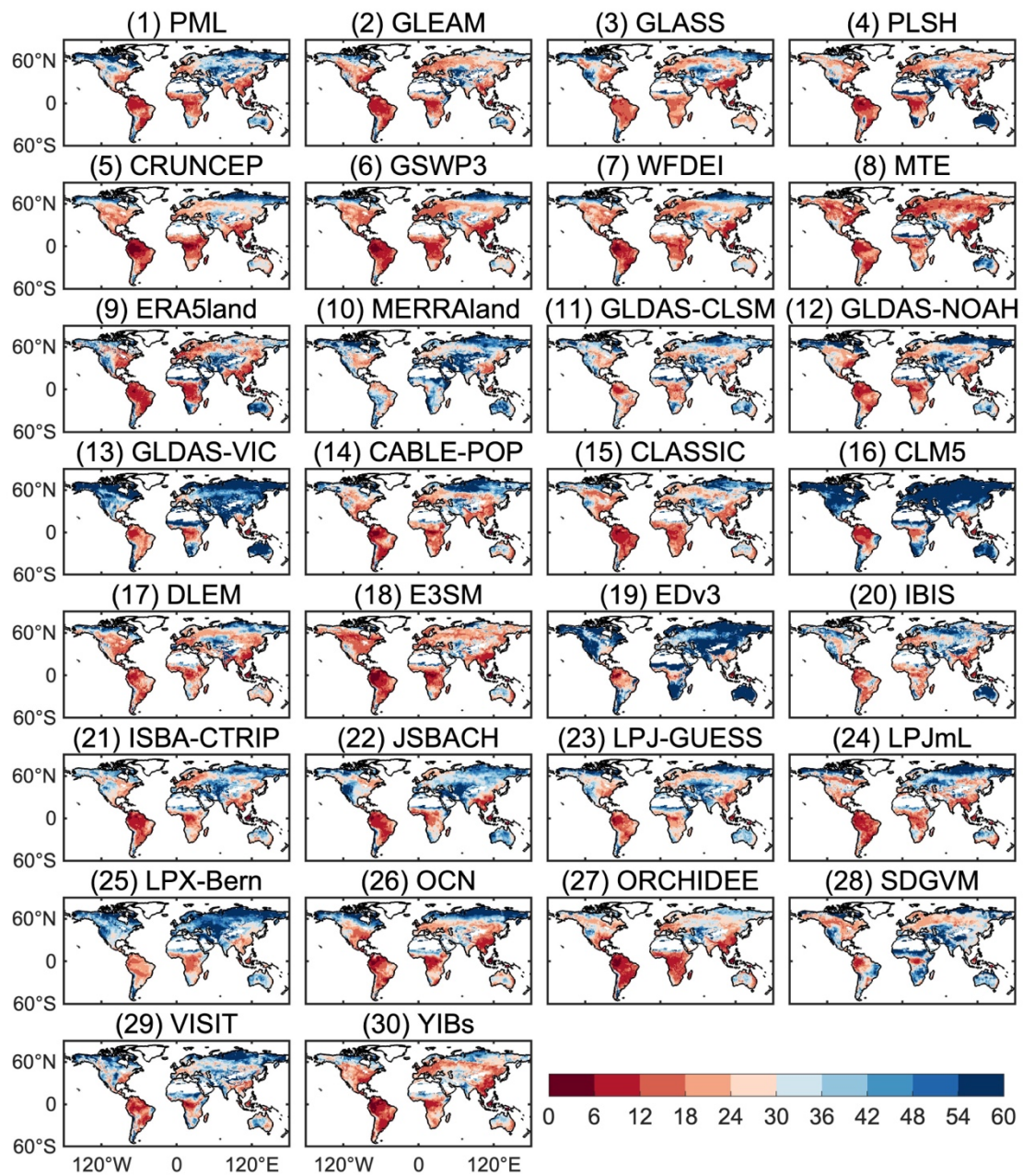
Fig. S22: Spatial distribution of relative uncertainty of TCH for each ET dataset on

monthly scale for the common coverage years from 1982 to 2011 (unit: %).

330

331

332

333

334

335
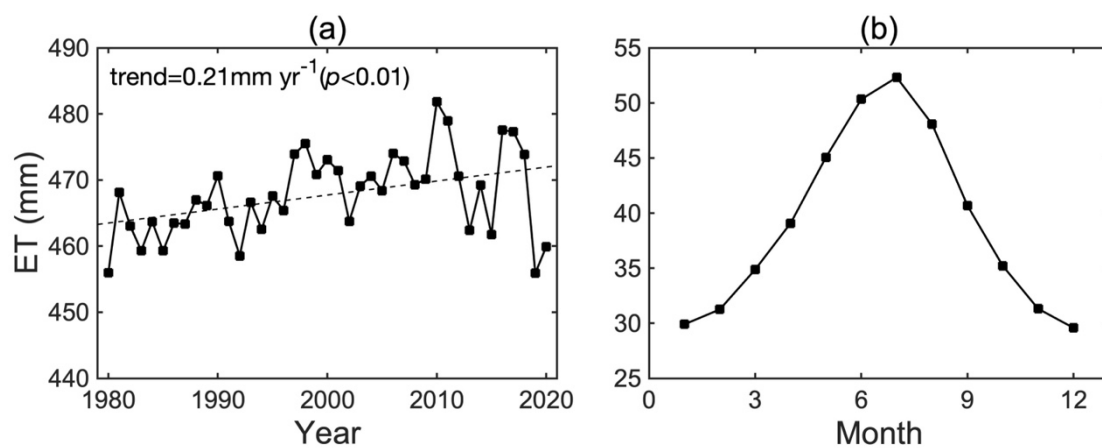
Fig. S23: Interannual and multi-year average seasonal variations of BMA-ET during

1980–2020.

338
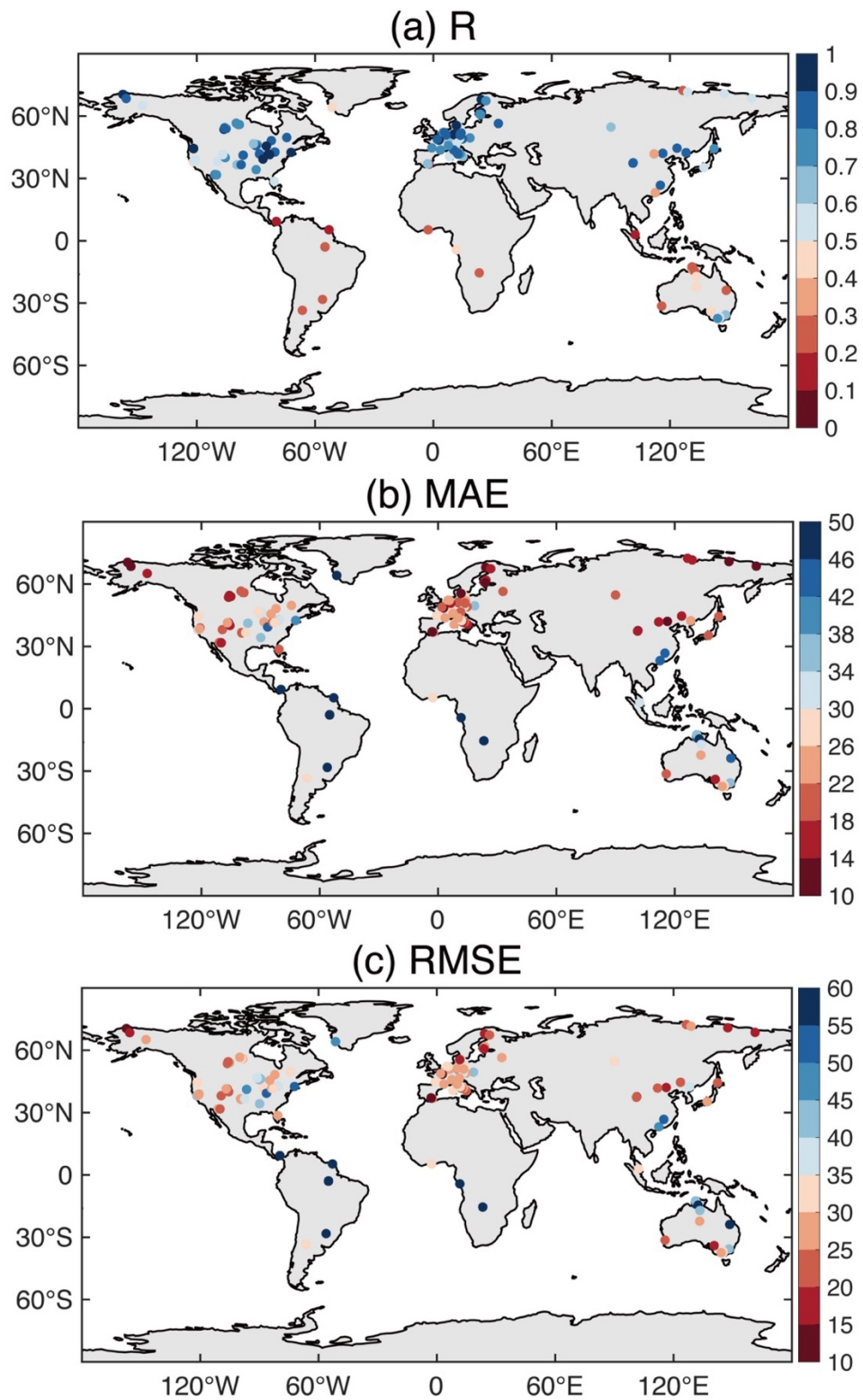
Fig. S24: Spatial distribution of correlation coefficient (R), mean absolute error (MAE) and root mean square error (RMSE) verified by BMA-ET and ET from FLUXNET from 1991 to 2011.
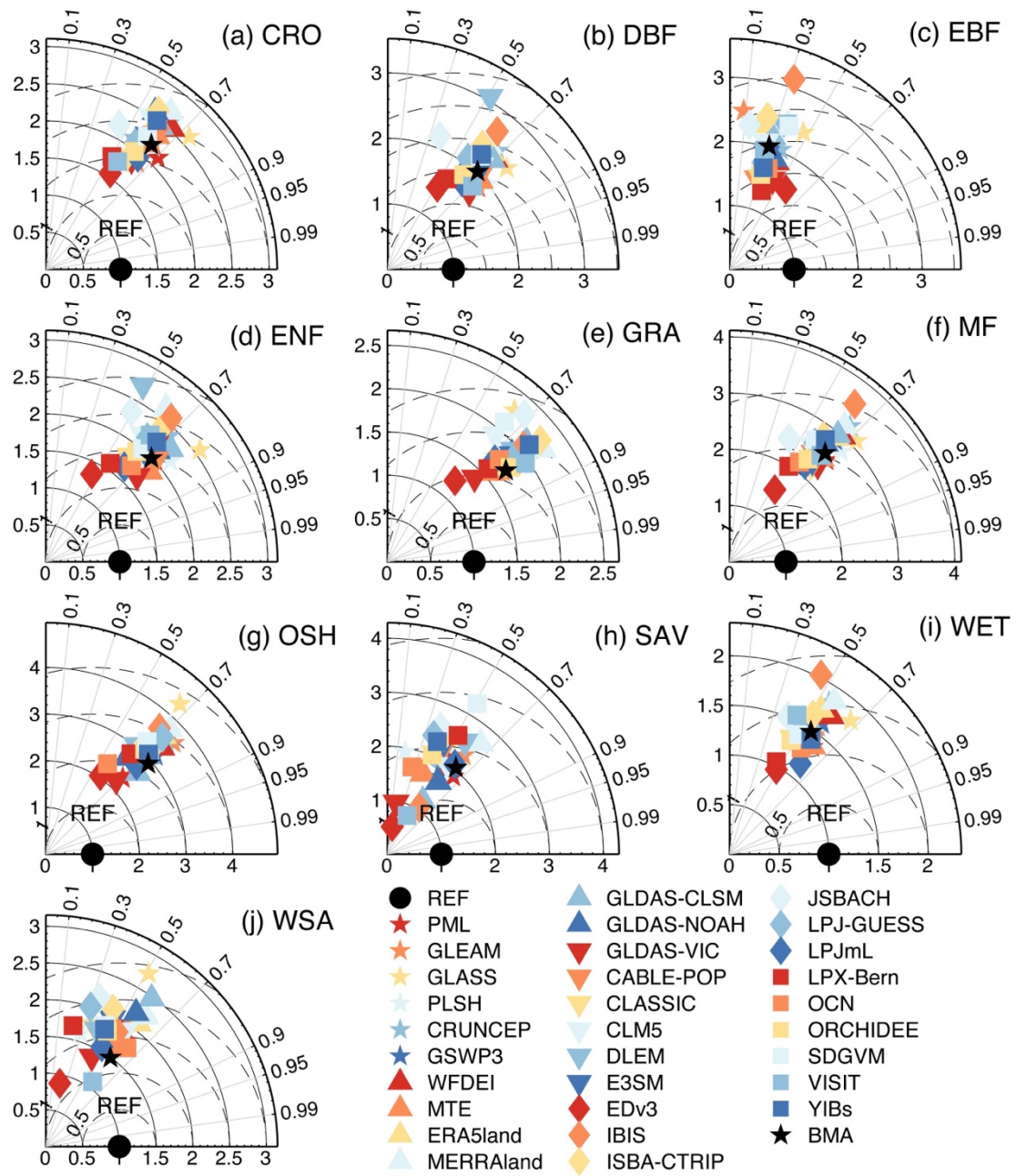
Fig. S25: Taylor diagram of ET datasets and BMA-ET at all sites under different vegetation types at monthly scale from 1991 to 2011. The observation data is ET from FLUXNET.
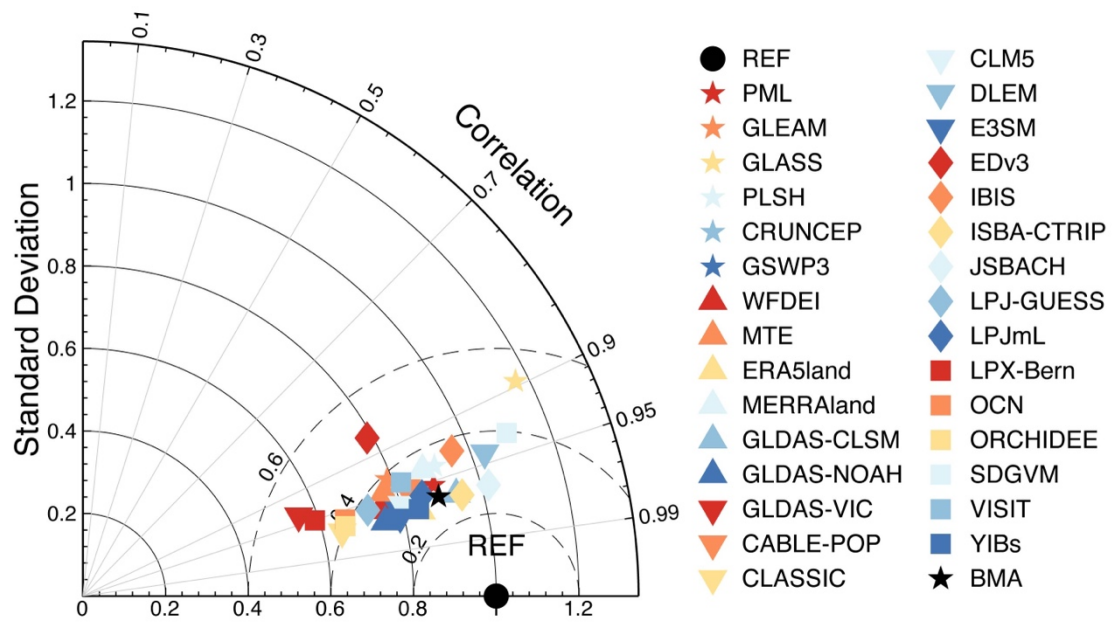
Fig. S26: Overall accuracy of all datasets and BMA-ET in simulating basin-scale evapotranspiration from 1982 to 2011.

355   **Table S1**. Data download links for evapotranspiration datasets.

ID	Name	Data download links
1	PML	https://doi.org/10.4225/08/5719A5C48DB85
2	GLEAM 3.6a	https://www.gleam.eu/#downloads
3	GLASS	http://www.glass.umd.edu/
4	PLSH	http://files.ntsg.umt.edu/data/ET_global_monthly/Global_8kmResolution/
5	FLUXCOM-CRUNCEP_v8	https://www.bgc-jena.mpg.de/geodb/projects/Data.php
6	FLUXCOM-GSWP3	https://www.bgc-jena.mpg.de/geodb/projects/Data.php
7	FLUXCOM-WFDEI	https://www.bgc-jena.mpg.de/geodb/projects/Data.php
8	MTE	https://www.bgc-jena.mpg.de/geodb/projects/DataDnld.php
9	ERA5-Land	https://cds.climate.copernicus.eu/datasets/reanalysis-era5-land-monthly-means?tab=download
10	MERRA-Land	https://gmao.gsfc.nasa.gov/reanalysis/MERRA-Land/data/
11	GLDAS CLSM 2.0	https://disc.gsfc.nasa.gov/datasets?keywords=GLDAS&page=1&source=Models%20Catchment-LSM
12	GLDAS NOAH 2.1	https://disc.gsfc.nasa.gov/datasets?keywords=GLDAS&page=1&source=Models%20Noah-LSM
13	GLDAS VIC	https://disc.gsfc.nasa.gov/datasets?keywords=GLDAS&page=1&source=Models%20VIC-LSM
14	CABLE-POP	https://blogs.exeter.ac.uk/trendy/protocol/
15	CLASSIC	https://blogs.exeter.ac.uk/trendy/protocol/
16	CLM5.0	https://blogs.exeter.ac.uk/trendy/protocol/
17	DLEM	https://blogs.exeter.ac.uk/trendy/protocol/
18	E3SM	https://blogs.exeter.ac.uk/trendy/protocol/

19	EDv3	https://blogs.exeter.ac.uk/trendy/protocol/
20	IBIS	https://blogs.exeter.ac.uk/trendy/protocol/
21	ISBA-CTRIP	https://blogs.exeter.ac.uk/trendy/protocol/
22	JSBACH	https://blogs.exeter.ac.uk/trendy/protocol/
23	LPJ-GUESS	https://blogs.exeter.ac.uk/trendy/protocol/
24	LPJmL	https://blogs.exeter.ac.uk/trendy/protocol/
25	LPX-Bern	https://blogs.exeter.ac.uk/trendy/protocol/
26	OCN	https://blogs.exeter.ac.uk/trendy/protocol/
27	ORCHIDEE	https://blogs.exeter.ac.uk/trendy/protocol/
28	SDGVM	https://blogs.exeter.ac.uk/trendy/protocol/
29	VISIT	https://blogs.exeter.ac.uk/trendy/protocol/
30	YIBs	https://blogs.exeter.ac.uk/trendy/protocol/

356

357 **Table S2**. Vegetation types to which ET from FLUXNET (174) belong and the number

358 of sites corresponding to each vegetation type.

ID	Name	Abbreviation	Number of sites
1	Croplands	CRO	16
2	Closed shrublands	CSH	2
3	Deciduous broadleaf forests	DBF	22
4	Deciduous needleleaf forests	DNF	1
5	Evergreen broadleaf forests	EBF	14
6	Evergreen needleleaf forests	ENF	42
7	Grasslands	GRA	33
8	Mixed forests	MF	9
9	Open shrublands	OSH	10
10	Savannas	SAV	3
11	Wetlands	WET	16
12	Woody savannas	WSA	6

359

360

362 **Table S3**. Vegetation types and time ranges for the 174 ET from FLUXNET used in
363 this study.

ID	Name	Latitude	Longitude	IGBP	Start year	End year
1	AR-SLu	−33.4648	−66.4598	MF	2009	2011
2	AR-Vir	−28.2395	−56.1886	ENF	2009	2012
3	AT-Neu	47.1167	11.3175	GRA	2002	2012
4	AU-ASM	−22.283	133.249	SAV	2010	2014
5	AU-Ade	−13.0769	131.1178	WSA	2007	2009
6	AU-Cpr	−34.0021	140.5891	SAV	2010	2014
7	AU-Cum	−33.6152	150.7236	EBF	2012	2014
8	AU-DaP	−14.0633	131.3181	GRA	2007	2013
9	AU-Emr	−23.8587	148.4746	GRA	2011	2013
10	AU-Fog	−12.5452	131.3072	WET	2006	2008
11	AU-Gin	−31.3764	115.7138	WSA	2011	2014
12	AU-How	−12.4943	131.1523	WSA	2001	2014
13	AU-RDF	−14.5636	132.4776	WSA	2011	2013
14	AU-Rig	−36.6499	145.5759	GRA	2011	2014
15	AU-Stp	−17.1507	133.3502	GRA	2008	2014
16	AU-TTE	−22.287	133.64	GRA	2012	2014
17	AU-Tum	−35.6566	148.1517	EBF	2001	2014
18	AU-Wac	−37.4259	145.1878	EBF	2005	2008
19	AU-Whr	−36.6732	145.0294	EBF	2011	2014
20	AU-Wom	−37.4222	144.0944	EBF	2010	2014
21	AU-Ync	−34.9893	146.2907	GRA	2012	2014
22	BE-Bra	51.3076	4.5198	MF	1996	2014
23	BE-Lon	50.5516	4.7462	CRO	2004	2014
24	BE-Vie	50.3049	5.9981	MF	1996	2014
25	BR-Sa1	−2.8567	−54.9589	EBF	2002	2011
26	BR-Sa3	−3.018	−54.9714	EBF	2000	2004
27	CA-Gro	48.2167	−82.1556	MF	2003	2014
28	CA-Man	55.8796	−98.4808	ENF	1994	2008
29	CA-NS1	55.8792	−98.4839	ENF	2001	2005

30	CA-NS2	55.9058	−98.5247	ENF	2001	2005
31	CA-NS3	55.9117	−98.3822	ENF	2001	2005
32	CA-NS4	55.9144	−98.3806	ENF	2002	2005
33	CA-NS5	55.8631	−98.485	ENF	2001	2005
34	CA-NS6	55.9167	−98.9644	OSH	2001	2005
35	CA-NS7	56.6358	−99.9483	OSH	2002	2005
36	CA-Oas	53.6289	−106.1978	DBF	1996	2010
37	CA-Obs	53.9872	−105.1178	ENF	1997	2010
38	CA-Qfo	49.6925	−74.3421	ENF	2003	2010
39	CA-SF1	54.485	−105.8176	ENF	2003	2006
40	CA-SF2	54.2539	−105.8775	ENF	2001	2005
41	CA-SF3	54.0916	−106.0053	OSH	2001	2006
42	CA-TP1	42.6609	−80.5595	ENF	2002	2014
43	CA-TP2	42.7744	−80.4588	ENF	2002	2007
44	CA-TP3	42.7068	−80.3483	ENF	2002	2014
45	CA-TP4	42.7102	−80.3574	ENF	2002	2014
46	CA-TPD	42.6353	−80.5577	DBF	2012	2014
47	CG-Tch	−4.2892	11.6564	SAV	2006	2009
48	CH-Cha	47.2102	8.4104	GRA	2005	2014
49	CH-Dav	46.8153	9.8559	ENF	1997	2014
50	CH-Fru	47.1158	8.5378	GRA	2005	2014
51	CH-Lae	47.4783	8.3644	MF	2004	2014
52	CH-Oe1	47.2858	7.7319	GRA	2002	2008
53	CH-Oe2	47.2864	7.7337	CRO	2004	2014
54	CN-Cha	42.4025	128.0958	MF	2003	2005
55	CN-Cng	44.5934	123.5092	GRA	2007	2010
56	CN-Din	23.1733	112.5361	EBF	2003	2005
57	CN-Du2	42.0467	116.2836	GRA	2006	2008
58	CN-Ha2	37.6086	101.3269	WET	2003	2005
59	CN-HaM	37.37	101.18	GRA	2002	2004
60	CN-Qia	26.7414	115.0581	ENF	2003	2005
61	CN-Sw2	41.7902	111.8971	GRA	2010	2012
62	CZ-BK1	49.5021	18.5369	ENF	2004	2014

63	CZ-BK2	49.4944	18.5429	GRA	2004	2012
64	CZ-wet	49.0247	14.7704	WET	2006	2014
65	DE-Akm	53.8662	13.6834	WET	2009	2014
66	DE-Geb	51.0997	10.9146	CRO	2001	2014
67	DE-Gri	50.95	13.5126	GRA	2004	2014
68	DE-Hai	51.0792	10.4522	DBF	2000	2012
69	DE-Kli	50.8931	13.5224	CRO	2004	2014
70	DE-Lkb	49.0996	13.3047	ENF	2009	2013
71	DE-Lnf	51.3282	10.3678	DBF	2002	2012
72	DE-Obe	50.7867	13.7213	ENF	2008	2014
73	DE-RuR	50.6219	6.3041	GRA	2011	2014
74	DE-RuS	50.8659	6.4471	CRO	2011	2014
75	DE-Seh	50.8706	6.4497	CRO	2007	2010
76	DE-SfN	47.8064	11.3275	WET	2012	2014
77	DE-Spw	51.8922	14.0337	WET	2010	2014
78	DE-Tha	50.9626	13.5651	ENF	1996	2014
79	DK-Eng	55.6905	12.1918	GRA	2005	2008
80	DK-Sor	55.4859	11.6446	DBF	1996	2014
81	ES-Amo	36.8336	−2.2523	OSH	2007	2012
82	ES-LJu	36.9266	−2.7521	OSH	2004	2013
83	ES-LgS	37.0979	−2.9658	OSH	2007	2009
84	FI-Hyy	61.8474	24.2948	ENF	1996	2014
85	FI-Jok	60.8986	23.5134	CRO	2000	2003
86	FI-Let	60.6418	23.9595	ENF	2009	2012
87	FI-Lom	67.9972	24.2092	WET	2007	2009
88	FI-Sod	67.3624	26.6386	ENF	2001	2014
89	FR-Fon	48.4764	2.7801	DBF	2005	2014
90	FR-Gri	48.8442	1.9519	CRO	2004	2014
91	FR-LBr	44.7171	−0.7693	ENF	1996	2008
92	FR-Pue	43.7413	3.5957	EBF	2000	2014
93	GF-Guy	5.2788	−52.9249	EBF	2004	2014
94	GH-Ank	5.2685	−2.6942	EBF	2011	2014
95	GL-NuF	64.1308	−51.3861	WET	2008	2014

96	IT-BCi	40.5237	14.9574	CRO	2004	2014
97	IT-CA1	42.3804	12.0266	DBF	2011	2014
98	IT-CA2	42.3772	12.026	CRO	2011	2014
99	IT-CA3	42.38	12.0222	DBF	2011	2014
100	IT-Col	41.8494	13.5881	DBF	1996	2014
101	IT-Cp2	41.7043	12.3573	EBF	2012	2014
102	IT-Cpz	41.7052	12.3761	EBF	1997	2009
103	IT-La2	45.9542	11.2853	ENF	2000	2002
104	IT-Lav	45.9562	11.2813	ENF	2003	2014
105	IT-MBo	46.0147	11.0458	GRA	2003	2013
106	IT-Noe	40.6062	8.1517	CSH	2004	2014
107	IT-PT1	45.2009	9.061	DBF	2002	2004
108	IT-Ren	46.5869	11.4337	ENF	1998	2013
109	IT-Ro1	42.4081	11.93	DBF	2000	2008
110	IT-Ro2	42.3903	11.9209	DBF	2002	2012
111	IT-SRo	43.7279	10.2844	ENF	1999	2012
112	IT-Tor	45.8444	7.5781	GRA	2008	2014
113	JP-MBF	44.3869	142.3186	DBF	2003	2005
114	JP-SMF	35.2617	137.0788	MF	2002	2006
115	MY-PSO	2.973	102.3062	EBF	2003	2009
116	NL-Hor	52.2403	5.0713	GRA	2004	2011
117	NL-Loo	52.1666	5.7436	ENF	1996	2014
118	PA-SPn	9.3181	−79.6346	DBF	2007	2009
119	PA-SPs	9.3138	−79.6314	GRA	2007	2009
120	RU-Che	68.613	161.3414	WET	2002	2005
121	RU-Cok	70.8291	147.4943	OSH	2003	2014
122	RU-Fyo	56.4615	32.9221	ENF	1998	2014
123	RU-Ha1	54.7252	90.0022	GRA	2002	2004
124	RU-Sam	72.3738	126.4958	GRA	2002	2014
125	RU-SkP	62.255	129.168	DNF	2012	2014
126	RU-Tks	71.5943	128.8878	GRA	2010	2014
127	SE-St1	68.3541	19.0503	WET	2012	2014
128	US-AR1	36.4267	−99.42	GRA	2009	2012

129	US-AR2	36.6358	−99.5975	GRA	2009	2012
130	US-ARM	36.6058	−97.4888	CRO	2003	2012
131	US-Atq	70.4696	−157.4089	WET	2003	2008
132	US-Blo	38.8953	−120.6328	ENF	1997	2007
133	US-CRT	41.6285	−83.3471	CRO	2011	2013
134	US-Cop	38.09	−109.39	GRA	2001	2007
135	US-GBT	41.3658	−106.2397	ENF	1999	2006
136	US-GLE	41.3665	−106.2399	ENF	2004	2014
137	US-Goo	34.2547	−89.8735	GRA	2002	2006
138	US-Ha1	42.5378	−72.1715	DBF	1991	2012
139	US-IB2	41.8406	−88.241	GRA	2004	2011
140	US-Ivo	68.4865	−155.7503	WET	2004	2007
141	US-KS2	28.6086	−80.6715	CSH	2003	2006
142	US-Los	46.0827	−89.9792	WET	2000	2014
143	US-MMS	39.3232	−86.4131	DBF	1999	2014
144	US-Me2	44.4523	−121.5574	ENF	2002	2014
145	US-Me3	44.3154	−121.6078	ENF	2004	2009
146	US-Me4	44.4992	−121.6224	ENF	1996	2000
147	US-Me5	44.4372	−121.5668	ENF	2000	2002
148	US-Me6	44.3233	−121.6078	ENF	2010	2014
149	US-Myb	38.0499	−121.765	WET	2010	2014
150	US-NR1	40.0329	−105.5464	ENF	1998	2014
151	US-Ne1	41.1651	−96.4766	CRO	2001	2013
152	US-Ne2	41.1649	−96.4701	CRO	2001	2013
153	US-Ne3	41.1797	−96.4397	CRO	2001	2013
154	US-Oho	41.5545	−83.8438	DBF	2004	2013
155	US-PFa	45.9459	−90.2723	MF	1995	2014
156	US-Prr	65.1237	−147.4876	ENF	2010	2014
157	US-SRC	31.9083	−110.8395	OSH	2008	2014
158	US-SRG	31.7894	−110.8277	GRA	2008	2014
159	US-SRM	31.8214	−110.8661	WSA	2004	2014
160	US-Sta	41.3966	−106.8024	OSH	2005	2009
161	US-Syv	46.242	−89.3477	MF	2001	2014

162	US-Ton	38.4309	−120.966	WSA	2001	2014
163	US-Tw1	38.1074	−121.6469	WET	2012	2014
164	US-Twt	38.1087	−121.6531	CRO	2009	2014
165	US-UMB	45.5598	−84.7138	DBF	2000	2014
166	US-UMd	45.5625	−84.6975	DBF	2007	2014
167	US-Var	38.4133	−120.9508	GRA	2000	2014
168	US-WCr	45.8059	−90.0799	DBF	1999	2014
169	US-WPT	41.4646	−82.9962	WET	2011	2013
170	US-Whs	31.7438	−110.0522	OSH	2007	2014
171	US-Wi3	46.6347	−91.0987	DBF	2002	2004
172	US-Wi4	46.7393	−91.1663	ENF	2002	2005
173	US-Wkg	31.7365	−109.9419	GRA	2004	2014
174	ZM-Mon	−15.4391	23.2525	DBF	2000	2009

364

365

366   **Table S4**. The variable information from ET from FLUXNET used in this study.

ID	Variable name	Full name of variable
1	P_F	Precipitation
2	LE_F_MDS	Latent heat flux
3	H_F_MDS	Sensible heat flux
4	G_F_MDS	Soil heat flux
5	RH	Relative humidity
6	NETRAD	Net radiation

367

368

369 **Table S5**. Basin information.

ID	Basin name	Country	Station name	Station longitude	Station latitude	Starting and ending year
1	Amazon	Brazil	Obidos	−55.51	−1.95	1927–2018
2	Amur	Russia	Komsomolsk	137.00	50.53	1900–2006
3	Churchill	Canada	Churchill River	−94.62	58.12	1928–2013
4	Columbia	USA	The Dalles	−121.17	45.61	1900–2018
5	Congo	Congo	Kinshasa	15.30	−4.30	1903–2010
6	Danube	Romania	Ceatal Izma	28.73	45.22	1900–2010
7	Don	Russia	Razdorskaya	40.65	47.53	1881–2010
8	Fraser	Canada	Hope	−121.45	49.38	1912–2016
9	Huaihe	China	Bengbu	117.37	32.94	1915–2004
10	Kolyma	Russia	Kolymskoye	158.72	68.73	1927–2008
11	Lena	Russia	Kusur	127.39	70.68	1934–2011
12	MacKenzie	Canada	Arctic Red	−133.74	67.46	1943–2016
13	Mekong	Laos	Pakse	105.80	15.11	1923–2005
14	Mississippi	USA	Vicksburg	−90.91	32.31	1928–2018
15	Nelson	Canada	Upstream of Bladder	−97.92	54.77	1915–2016
16	Niger	Nigeria	Lokoja	6.77	7.80	1915–2012
17	Ob'	Russia	Salekhard	66.60	66.63	1930–2015
18	Orange	South Africa	Vioolsdrift	17.63	−28.78	1935–2018
19	Ottawa	Canada	Chats Falls	−76.23	45.47	1914–2018
20	Paraná	Argentina	Timbues	−60.71	−32.67	1905–2018
21	Parnaiba	Brazil	Porto Formo	−42.37	−3.46	1955–2018
22	Pechora	Russia	Oksino	52.18	67.63	1916–2014
23	Rhine	Netherlands	Lobith	6.11	51.85	1901–2017
24	Saõ Francisco	Brazil	Traipu	−36.99	−9.98	1926–2018

25	Severnaya Dvina	Russia	Ust Pinega	41.92	64.13	1900–2014
26	Saint Lawrence	Canada	Cornwall ON	−74.74	45.00	1900–2018
27	Tocantins	Brazil	Tucurui	−49.67	−3.76	1955–2018
28	Uruguay	Argentina	Concordia	−58.03	−31.40	1942–2018
29	Yangtze	China	Datong	117.62	30.77	1960–2016
30	Yellow River	China	Lijin	118.25	37.50	1960–2014
31	Yenisei	Russia	Igarka	86.48	67.43	1936–2015
32	Yukon	USA	Pilot Station	−162.88	61.93	1956–2018

370

371